# Analysis of translating mitoribosome reveals functional characteristics of protein synthesis in mitochondria of fungi

Yuzuru Itoh[1,2†], Andreas Naschberger[1†], Narges Mortezaei[1†], Johannes Herrmann[3] and Alexey Amunts[1,2*]

[1]Science for Life Laboratory, Department of Biochemistry and Biophysics, Stockholm University, 17165 Solna, Sweden

[2]Department of Medical Biochemistry and Biophysics, Karolinska Institutet, 17165 Solna, Sweden

[3]Cell Biology, University of Kaiserslautern, Erwin-Schrödinger-Straße 13, 67663 Kaiserslautern, Germany

† These authors contributed equally to this work.

* email: amunts@scilifelab.se

**Abstract**

Mitoribosomes have been specialized for protein synthesis in mitochondria. However, the structural basis for the mitoribosomal mechanism of action is not understood. We report models of the translating fungal mitoribosome with mRNA, tRNA and nascent polypeptide, as well as an assembly intermediate. Mitochondria-specific rRNA and protein elements coordinate binding of nicotinamide adenine dinucleotide (NAD) in the central protuberance of the large subunit and the ATPase inhibitory factor 1 ($IF_1$) in the small subunit. The models of the active fungal mitoribosome explain how mRNA binds through a dedicated protein platform on the small subunit, tRNA is translocated with the help of newly identified protein mL108, bridging it with L1 stalk on the large subunit, and nascent polypeptide paths through a newly shaped exit tunnel involving a series of structural rearrangements. An assembly intermediate is modeled with the maturation factor Atp25, providing insight in to the biogenesis of the mitoribosomal large subunit and translation regulation.

Protein synthesis in mitochondria supports bioenergetics of eukaryotic cells and is executed by dedicated mitoribosomes. Cryo-EM has been instrumental in revealing the first structural snapshots of mitoribosomes. While for mammals the obtained models from human embryonic kidney cells[1,2] are in agreement with those from porcine and bovine tissues[3,4], the structure of the mitoribosome from the yeast *Saccharomyces cerevisiae* displayed considerable specializations[5,6]. Particularly, it proposed a distinct composition and putative deviations in the functionally defining features of translation, including an expanded mRNA channel exit and rerouted polypeptide exit channel. Although the existing cryo-EM data is informative, the deviations of the mitoribosome from a single-celled *S. cerevisiae* that lacks complex I are more likely species-specific and therefore cannot be considered as a prototypic example. In addition, the available models are incomplete due to the limited resolution. Functionally, since the models were derived from dormant mitoribosomes, without tRNA bound to mRNA and nascent polypeptide, the mechanism of action and roles of specific proteins could not be understood. Therefore, in the absence of high-resolution structural information of the translating mitoribosome, key questions regarding mitochondrial translation remain open. To provide a representative reference for studying protein synthesis in the mitochondria of fungi, and to reveal how the mitoribosome functions in coordination with its translation partners, we determined structures of the translating mitoribosome from the representative fungal model organism *Neurospora crassa.*

*N. crassa* has been recognized as the organism used for answering a variety of fundamental biological questions in the field of mitochondrial translation, and low resolution reconstruction of the mitoribosome was reported[7]. Other contributions of this model organism include early characterization of the physicochemical properties of the mitoribosomes and the base composition of its rRNA[8], the finding that mitoribosomal intactness requires a relatively high magnesium concentration[9], studies showing radioactive amino acid incorporation into mitoribosome[10], and the finding that Oxa1 facilitates integration of mitochondrially encoded proteins into the inner membrane[11]. Therefore, to provide a reference for the process of protein synthesis in mitochondria, we set out to investigate the functional translation apparatus from the model organism *N. crassa.*

## Structure determination

In order to characterize a representative functional mitoribosome, the *N. crassa* mycelia of the strain K5-15-23-1 overexpressing the protein Oxa1[11] were grown aerobically and translation was stalled using chloramphenicol prior to harvesting. The mycelia were dried, lysed with mortar and pestle, and the mitoribosomes were purified as described previously[12], and subjected to cryo-EM analysis. The cryo-EM consensus map was obtained from 131,806 particles at overall resolution of 2.86 Å (Supplementary Fig. 1 and Supplementary Table 1).

The 3D classification resulted in two reconstructions of the mitoribosome corresponding to the ratcheted and non-ratcheted states (Supplementary Fig. 1). After subtracting the mitoribosome signals outside the tRNA binding sites, followed by focused 3D classifications, we obtained three distinct classes of mitoribosomes with a tRNA occupying P-site (P/P), E-site (E/E), and in the hybrid P/E state, at the overall resolutions of 3.05, 3.10, and 2.99 Å, respectively (Supplementary

Fig. 1). In the P/P and P/E tRNA states, we detected and modeled co-purified native mitochondrial mRNA, and the density corresponding to the nascent polypeptide was identified in the P/P tRNA state.

To further improve the local resolution, focused masked refinements were performed using the masks for the large subunit (mtLSU) core, central protuberance (CP), L1 stalk, uL10m region, the small subunit (mtSSU) head, body and tail (Supplementary Figs. 2-5). Consequently, the resolution was improved to ~2.50-3.40 Å throughout most of the regions. The quality of the maps allowed building the most complete available model, including identification of five proteins previously missed: uL1m, uL10m, uL11m, mL53, and mL54; two newly identified mitoribosomal proteins: mL108 and the ATP synthase inhibitory factor 1 ($IF_1$); and 60 proteins with higher completeness, as well as the rRNAs (Fig. 1a, Supplementary Figs 6-9).

In addition, we noted that mitoribosomes from actively growing *N. crassa* mycelia contain a pool of free mtLSU (Supplementary Fig. 5), which resembles the profile of the assembly intermediate reported from the mitochondria of human embryonic kidney cells[13]. Unlike the mtLSU in the intact mitoribosome, this population is missing the density for bL9m, but has an extra factor Atp25 bound to uL14m, and a poor density at the interface consistent with unfolded mt-rRNA. The quality of the structural data allowed the analysis of the differences with the mature mtLSU, and to propose a putative regulatory mechanism.

**Overall structure and new features**

The fungal mitoribosome consists of 78 different proteins, 23S and 16S rRNAs (Fig. 1, Supplementary Figs 6-9, Supplementary Tables 2 and 3). The proteins mS42 and $IF_1$ are found in two copies as homodimers. 48 bacterial orthologs are extended, and 30 proteins are mitochondria-specific. For the rRNA, we modeled 16 expansion segments (ES), 15 of which are in the mtLSU (Supplementary Figs. 6-8), and several other rRNA regions have been reduced. The deletion in the mtDNA genome are not correlated with a specific functional feature or attributed to selective loss/gain of activity, but rather reflect a general reductive phase in the mitochondrial genome[7]. For the native mitochondrial tRNAs (P/P, P/E, E/E states) and mRNA, we modeled nucleotide sequences that fit the corresponding densities the best, because those densities represent a mixture of different tRNAs and mRNAs in mitochondria.

Some of the improvements in the model due to the high-resolution map are exemplified in Figure 1. Protein mS27, which was previously partially built as poly-Ala, has been identified directly from the density as a helical repeat protein consistent with mammalian counterparts. We named it accordingly mS27 (previously mS44) (Fig. 1b, Supplementary Fig. 10 and Supplementary Table 3). Another example is the protein mS29 that was reported as a GTPase involved in apoptosis, and mutations in the P-loop motif of the nucleotide binding pocket were suggested to impair this function[14]. In the nucleotide pocket of mS29, which was previously modeled with guanosine diphosphate (GDP), we can see at the local resolution of 2.77 Å that the density for N2 purine ring atom is missing, and the correct assignment for the nucleotide is adenosine triphosphate (ATP) (Fig. 1b). This is further supported by the better resolved chemical environment formed by Leu150

of mS29, which would be incompatible with guanine since the O6 carbonyl of guanine imparts repulsive interaction with the backbone carbonyl of Leu150 (acceptor with acceptor), and the NH1 group of guanine forms a second repulsive interaction with the backbone NH group of Leu150 (donor with donor). Placing an ATP instead of GDP leads to more favorable interactions. Therefore, the structure shows no evidence of mS29 being a GTPase in fungi.

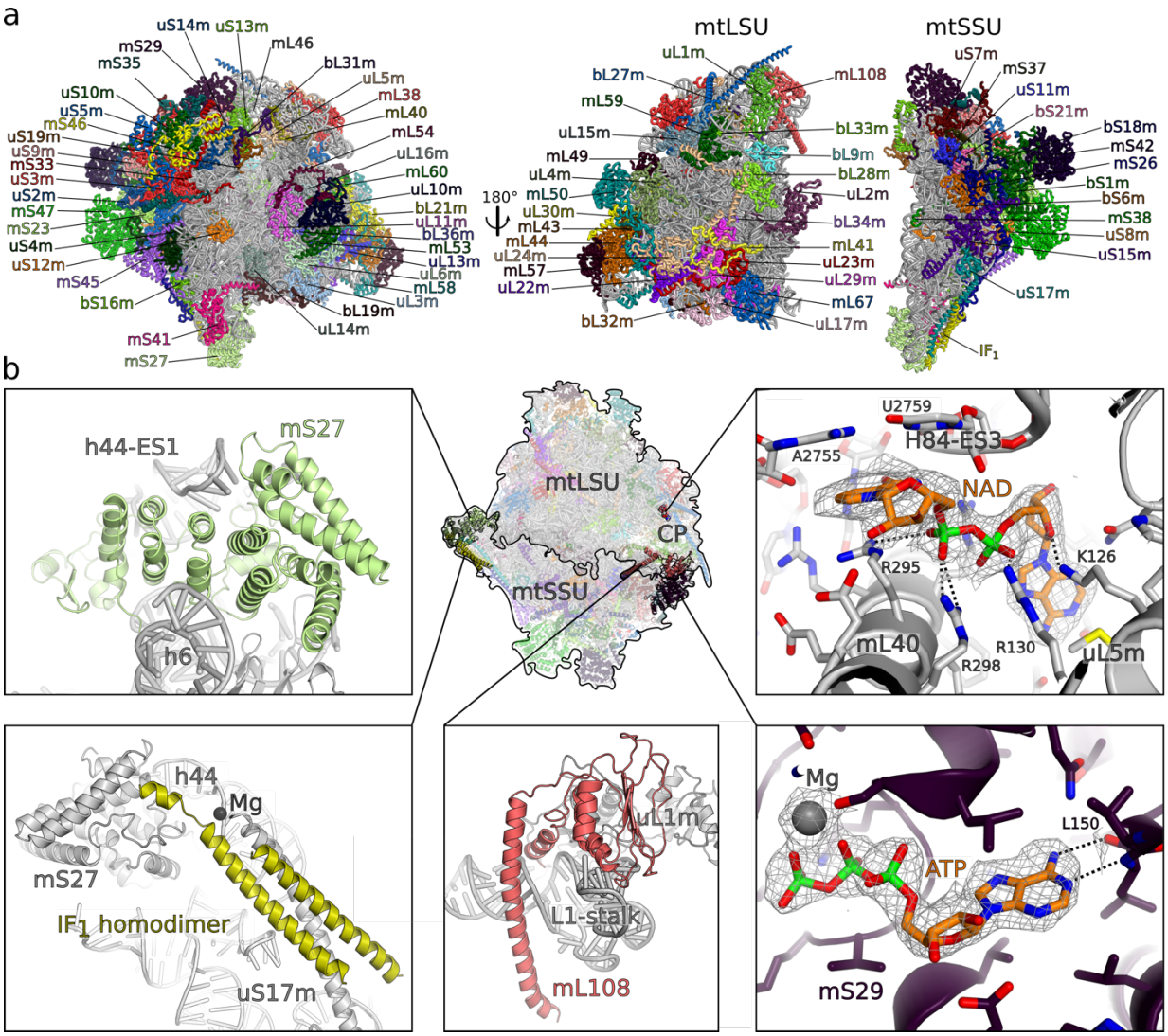


**Figure 1: Structure of the fungal mitoribosome and new features.** a, Overall structure of the complete mitoribosome and its subunits with indicated mitoribosomal proteins. b, Examples of newly identified features. Remodeled and reannotated mS27 interacts with h44-ES1. Newly identified mitoribosomal component $IF_1$ homodimer bound to h44-ES1 and uS17m extension. NAD binding pocket in the CP formed by uL5m, mL40, and H84-ES3. Newly identified mitoribosomal component mL108 is located in the L1 stalk. Nucleotide binding pocket of mS29 bound with chemically favorable ATP shown with its density.

In the CP, we found NAD in the binding pocket formed by mL40, uL5m, and rRNA H84-ES3 (Fig. 1b). Positively charged residues of mL40 and uL5m interact with the negatively charged NAD phosphates. The pyridine ring of the nicotinamide is held in place by π-stacking on the base pair of

A2755 and U2759. Arg295 of mL40 forms π-stacking at the other side of the NAD pyridine. Therefore, NAD bridges the mitoribosomal proteins and the mt-rRNA at the core of CP. This implies regulatory function in the assembly of the mtLSU based on the local NAD level.

In the mtSSU tail, we found the natural inhibitor of the mitochondrial ATP synthase $IF_1$ bound as a homodimer (Fig. 1b). It has been identified unambiguously from the side-chain density (Supplementary Fig. 11a) and mass-spectrometry data (Supplementary Table 4). In the ATP synthase, $IF_1$ functions through inserting its N-terminal part into the catalytically active $F_1$-ATPase, thereby blocking its rotational movement and subsequently the ATP hydrolase activity[15,16]. In our structure of the mitoribosome, $IF_1$ coiled-coil forms a helical bundle with the C-terminal extension of uS17m and also binds to mS27 and h44 rRNA (Fig. 1b, Supplementary Fig. 11). It is also bridged through a metal ion $Mg^{2+}$, coordinated by uS17m Q162 and the backbone phosphate of h44 A1745 (Supplementary Fig. 11c). The topology of $IF_1$ homodimer is such that the C-terminus of each monomer points in the opposite direction: one towards the mtSSU body, and the other towards the solvent. Although the topology resembles that of the bovine $IF_1$ homodimer[17] (Supplementary Fig. 11a), the dimerization region is shifted ~7 residues toward the N-terminus and shorter by ~10 residues, suggesting it is less stable. In addition, against the sequence similarity with the yeast counterpart (Supplementary Fig. 11b), we find differences in topology when compared with the X-ray crystal structure of the *S. cerevisiae* $IF_1$ monomer bound to the $F_1$-ATPase[15] (Supplementary Fig. 11a). Particularly, the *S. cerevisiae* $IF_1$ has a short helix α1 followed by a longer helix α2, whereas in *N. crassa* the α1 counterpart region appears to be disordered, and α2 comprises two helices separated by 2 residues. The differences might also be affected by different binding partners (mitoribosome vs $F_1$-ATPase), reflecting the structural flexibility of $IF_1$. Since the C-terminal extension of uS17m stabilizing the $IF_1$ on the mitoribosome is specific to *N. crassa* (Supplementary Fig. 11c) the feature of $IF_1$ binding might also be specific. Our structural analysis shows that h44 is expanded in this region of the mitoribosome, which would suggest that $IF_1$ has been acquired through the mechanism of 'structural patching' to stabilize the rapidly evolving growth[18]. Functionally, $IF_1$ may link the biogenesis of the mitoribosome to the ATP synthesis assembly and inhibition.

**The mechanism of mRNA binding involves a dedicated protein platform**

Focused classifications on the tRNA binding sites yielded structures of three distinct classes with bound tRNA in P/P, P/E, E/E (Supplementary Fig. 1). The quality of the density allowed us to generate structural models of the translating mitoribosomal complexes with P/P and P/E tRNAs. The presence of tRNAs correlates with additional density lining the mRNA channel path, where a well resolved map allowed modeling of 11 nucleotides of the native mRNA. The codon-anticodon base pairings are observed in the density of the P/P and P/E states (Fig. 2). The decoding center is conserved, including the position of the flipped-out bases A1803 (A1492 in *E. coli*), A1804 (A1493) and G756 (G530), as well as the curvature in mRNA around h28. In addition to the modeled mRNA nucleotides in the channel, bulky density extends upstream to the channel entry

and downstream to its exit. Therefore, the map allows us to determine how mRNA binds to the mitoribosome and to trace its complete path.

The reference point to the channel entry is the universal site formed by uS3m, uS4m, and uS5m. Compared to the previously determined structures of the bacterial complex, mitochondrial mRNA is also bound by mitochondria-specific protein mS35. However, the density for the mRNA chain starts prior to the conventional entry. Particularly, following the density, we observe extended structure involving mitochondria-specific extensions of uS3m and uS5m that are held together at the mtSSU head by mS35 and mS46 (Fig. 2a). This architecture is coupled to the mRNA terminus, thereby suggesting a potential platform for its loading on to the mitoribosome. The formed loading platform narrows the entry site considerably, ensuring that the mRNA entering the channel is unpaired. Interestingly, two mitochondria-specific proteins, mS26 and mS35, extend along the mRNA channel from its entry region to the opposite mtSSU pole, where the exit site is, providing a structural continuum (Fig. 2b).

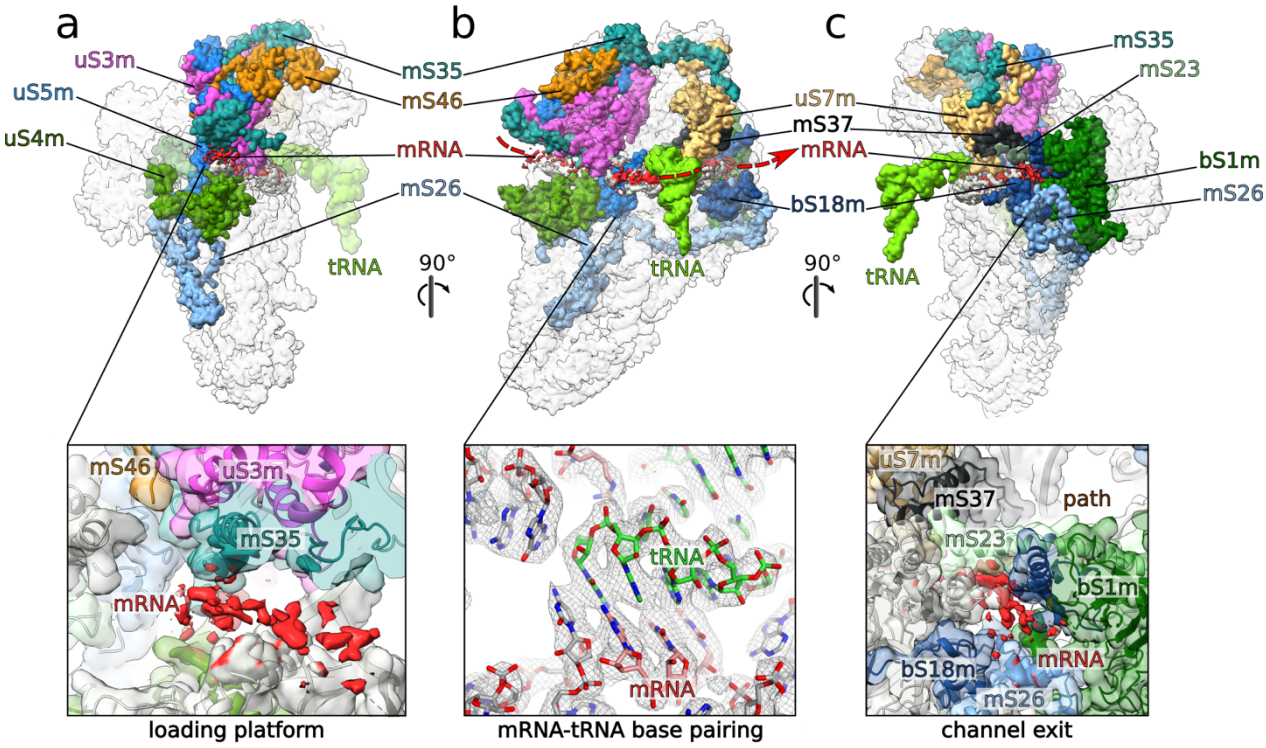


**Figure 2: The mRNA channel traced with the density.** a, The density for mRNA (red) reveals a protein platform formed by mS35, mS46 and extensions of uS3m and uS5m. b, The overall path taken by mRNA is indicated based on the additional density associated with the mtSSU, and codon-anticodon base pairings at the decoding center shown with density. c, At the exit site, proteins uS7m, bS18m, mS23, mS26, and mS37 are in contact with mRNA, and bS1m is permanently bound. A putative alternative path is indicated.

The channel exit site typically resides at the 3′ end of the rRNA. In the fungal mitoribosome, it has not been significantly altered. The remodeling reported in *S. cerevisiae* does not occur, and therefore represents either a dormant state or species-specific feature. In addition to the conserved proteins, mitochondria-specific mS23, mS26, and mS37 shape the path for mRNA movement (Fig.

193 2c). The C-terminal extension of uS7m narrows the channel, and protein bS18m, mS23, mS26, and
194 mS37 interact with the mRNA density directly. The path toward the exit appears to divaricate, and
195 each subway could in principle accommodate a single stranded mRNA. However, the density for
196 the 5′ mRNA clearly only follows the path lateral to mS26 that is also surrounded by a positively
197 charged chemical environment. Protein bS1m, which is considered to have one of the most
198 conserved and ancient protein domains with functional importance of unfolding mRNAs for active
199 translation[19], is permanently bound to the channel exit (Fig. 2c).
200

201 **The mechanism of tRNA translocation involves a new protein in L1 stalk**

202 During translation, tRNAs are translocated between the three sites. Upon peptide-bond formation,
203 the ribosomal subunits rotate with respect to each other, and the tRNA moves to the intermediate
204 hybrid state. The structure comparison between the complexes with P/P and P/E tRNAs reveals
205 sequential rearrangements in the network of mitoribosome-tRNA interactions and allows us to
206 determine how tRNA is translocated.

207 In the P/P state, the anticodon of the tRNA forms base pairing with the mRNA in the conserved P-
208 site of the mtSSU (Fig. 3 and Supplementary Fig. 12). Further stabilization is provided by the
209 conserved C-terminal Arg315 of uS9m, which forms salt bridges with the backbone phosphates in
210 the anticodon loop of the tRNA. The conserved H69 of mtLSU interacts with the D-arm of the
211 tRNA. The conformation of P/P tRNA is overall similar to bacteria. The A-site finger, known as a
212 functional attenuator and important for keeping the correct reading frame[20], takes in a straight
213 conformation forming the inter-subunit bridge B1a. The conserved G2453 (G2251) and G2454
214 (G2252) of the P-loop form base pairs with the CCA terminus of the tRNA and the emerging
215 peptide is bound to the terminal A76, waiting for peptidyl transfer to the next incoming aminoacyl-
216 tRNA at the A-site. Thus, the arrangement of structural elements and tRNA in mitochondria of
217 fungi shows a conserved P-site.

218 After peptide transfer occurs, the ribosomal subunits move relative to each other forming the
219 ratcheted conformation coupled with tRNA translocation, which is represented by our P/E hybrid
220 structure. In the ratcheted conformation, the L1 stalk moves to a closed conformation toward the
221 deacylated tRNA in the P/E hybrid state (Fig. 3). By masked refinement on L1 stalk, we improved
222 the density that allowed building its complete model for the first time in any mitoribosome. We
223 identified an additional protein component, namely mL108 (Fig. 1b and Supplementary Fig. 13),
224 which is an unprecedented occurrence in cytoplasmic counterparts. The core of the protein shows
225 a thioredoxin-like fold, which belongs to a small folding family of mitochondrial proteins mS25,
226 mL43, and the complex I subunit NDUFA2/B8, bearing the possibility of a shared evolutional
227 origin. The protein mL108 interacts with both the L1-stalk rRNA and the protein uL1m (Fig. 3).
228 Furthermore, it forms a new inter-subunit bridge with a long C-terminal helix (Fig. 3).

229 The bases A2381 (G2168) and C2348 (G2112) of the stalk rRNA stack on the elbow of the P/E
230 tRNA (Fig. 3). Unlike in bacteria, uL1m does not interact with the P/E tRNA, instead the domain
231 II of uL1m changes its conformation to form a mitoribsome-specific interaction with H82-ES1 in
232 the CP in the ratcheted state (Fig. 3). Therefore, the subunit rotation is synchronized with the L1

stalk movement during tRNA translocation. The terminal adenosine of the P/E tRNA inserts between the conserved G2873 (G2421) and A2874 (C2422) at the E site (Fig. 3). The anticodon arm of the tRNA remains located in the P-site forming the codon-anticodon base pairing with the mRNA resulting in distorted conformation to swing the acceptor arm into the E-site. The disordered N-terminal extension of mS29 gets structured in the ratcheted state and interacts to the minor groove of the anticodon stem of the P/E tRNA (Supplementary Fig. 12), suggesting mitochondria-specific regulation of the translation mechanism. The long C-terminal helix of mL108 reaches down to the mtSSU, applying an additional stabilization of the L1 stalk.

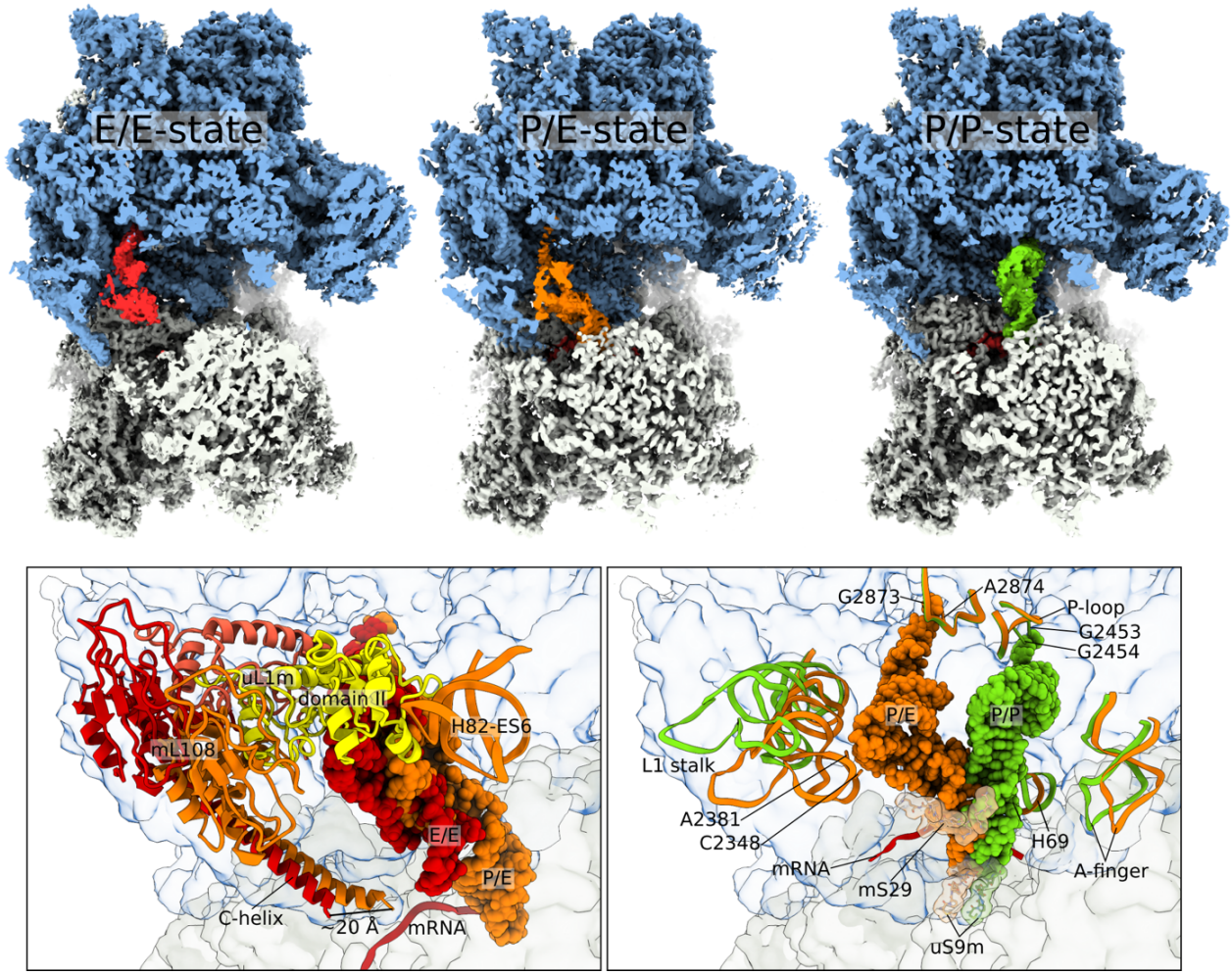


**Figure 3: Translocation of tRNA and the L1 stalk.** 3D reconstructions of the different states are shown in the top panel (mtLSU blue; mtSSU gray). Structural rearrangements upon transition between the three states are shown in the bottom panels (right: P/P to P/E; left: P/E to E/E). Each two states have been superimposed, and the affected structural elements are shown according to the text.

Upon back rotation of the mtSSU into the non-ratcheted E/E state, the L1 stalk moves outwards assisting to pull the P/E tRNA into the E/E state, allowing dissociation into the solvent to complete the translocation cycle (Fig. 3 and Supplementary Fig. 12). The protein uL1m thereby detaches

from the CP, releasing the domain II of uL1m. The tip of the C-terminal helix of mL108 translates ~20 Å forming a new bridge with mtSSU by slightly changing its curvature. This structural rearrangement during mtSSU rotation suggests a mitochondria-specific ratchet sensing mechanism that coordinates the movement of the mtSSU rotation via mL108 to the L1 stalk.

Taken together, the data enables to derive a mechanism for the tRNA translocation describing a series of key conformational changes of the mitoribosomes and its ligands. First, the L1 stalk interacts with mtSSU through mL108 thereby sensing the rotation state. This leads to the inward moving of the rRNA part of the L1 stalk to interact with the tRNA. The domain II of uL1m stabilizes the conformation through the mitochondria-specific interactions with the CP, and mS29 N-terminal loop becomes ordered and stabilizes the tRNA in the P/E state, which is disrupted in the following E/E state.

**The nascent polypeptide path to exit the mitoribosome is driven by mitochondria-encoded rRNA reorganisation**

As the small mitoribosomal subunit progresses toward the 3' end of the mRNA, the peptidyl transferase center transfers amino acids from tRNAs to the nascent chain, which emerges through the exit tunnel of the large subunit. Therefore, the polypeptide exit tunnel is the defining feature of protein synthesis, and it further facilitates initial folding[21]. Given the fundamental role, the architecture of the tunnel path is among the most conserved features of the ribosome[22]. Against this background, the *S. cerevisiae* mitoribosome structure showed a tunnel path that deviates from the bacterial counterpart, primarily due to rRNA H24 deletion[5]. Consequently, the original tunnel was blocked by a specific extension of the mitoribosomal protein uL23m. To what extent the reported structural changes around the mitoribosomal exit tunnel are representative remained an open question. Since the subset of mRNAs subjected to translation in mitochondria from *S. cerevisiae* and *N. crassa* is similar in the way that both organisms harbor genes that encode for membrane proteins, as well as the soluble mitoribosomal protein uS3m, our analysis reveals the evolutionary drivers for the mitoribosomal exit tunnel adaptation.

For the clarity of the analysis, we partition the tunnel in to two subparts, namely 'upper' that starts with the peptidyl transferase center (PTC) and ends with the uL4m-uL22m constriction site and 'lower' from the constriction site to exit. In our structure, the density for an endogenous polypeptide is detected and the involved structural elements at the upper part of the tunnel are conserved with respect to the geometrical parameters, such as the length (~30Å) and average radius (~5.3 Å) (Fig. 4a). The constriction site between the loops uL4m-uL22m is located 34 Å from the start of the tunnel, and the position correlates well with the *E. coli* ribosome. The density for the nascent polypeptide can be traced from the starting point at the PTC until the beginning of the lower part of the tunnel (Fig. 4b).

In the lower part, protein extensions (uL22m, uL23m, uL24m) cluster and occupy the conventional bacteria-like path interior. As a result, although a continuous channel can be traced to the surface of the mitoribosome, the minimal radius of the channel is decreased to 3.3 Å, which represents a considerable narrowing compared to ~6 Å across bacterial ribosomes[22] (Fig. 4c). These dimensions

are inconsistent with both the experimental and simulation results showing that the lower part of the tunnel is large enough to hold folded proteins[21,23]. We further find side chains that would obstruct the pathway, the majority of which belong to charged amino acids (Supplementary Fig. 14a). Such occupation would induce an electrostatic Coulomb potential that is inconsistent with hosting hydrophobic polypeptides. Therefore, although the structure maintains the path, the bias toward non-regulated protein growth in the hollow region suggests that the conventional bacteria-like lower part of the tunnel is unlikely to be functional.

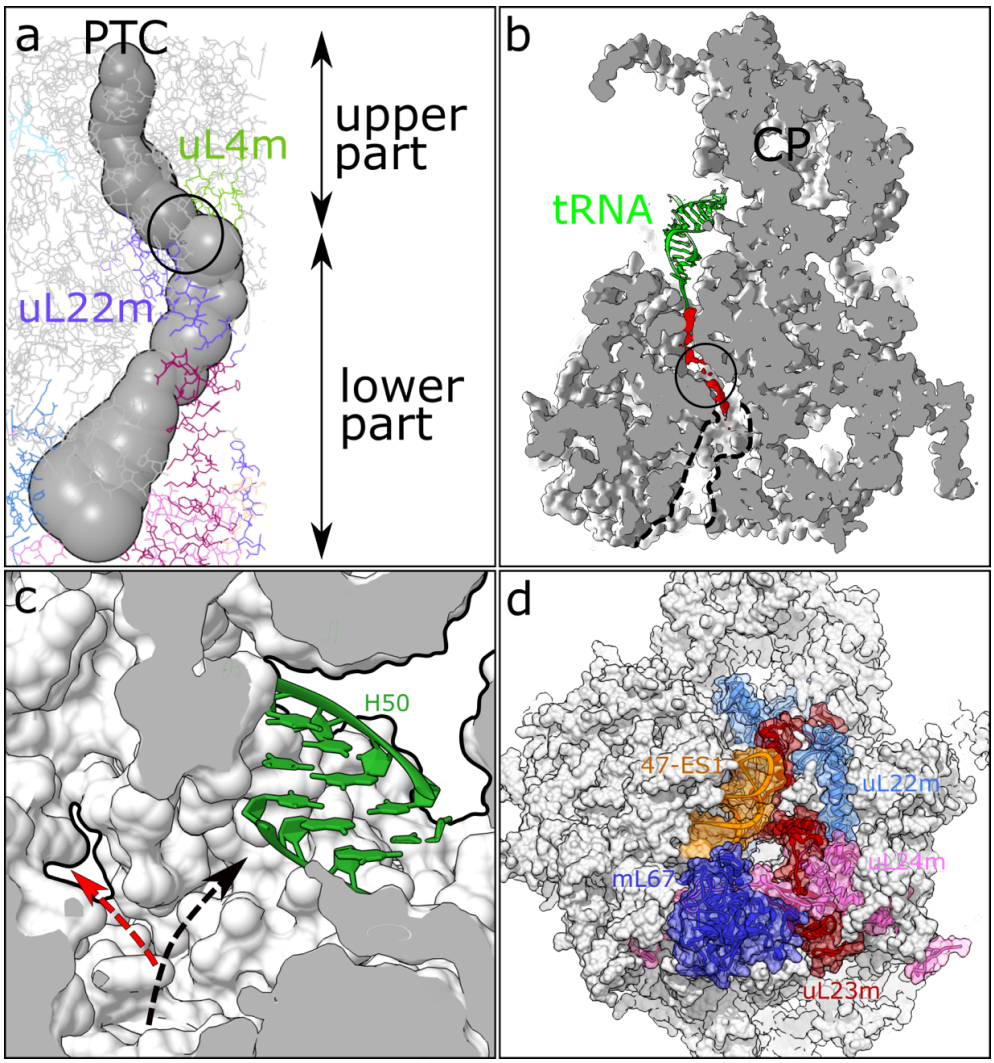


**Figure 4: The path of polypeptide of the mitoribosome from *N. crassa*.** a, The calculated tunnel showing the partition of the tunnel in to the upper and lower parts. The restriction site is surrounded by uL22m and uL4m and is labeled by the black circle. b, Cross-section of the large subunit showing the tunnel with density of the polypeptide reaching from the PTC until the beginning of the lower part of the tunnel. c, View of the branching point from inside the tunnel. The red arrow shows where the standard exit locates, which is restricted to 3.3 Å in *N. crassa*. The black arrow shows the path of the new tunnel, which was formed upon deletion of H50 which is shown in green. d, The view of the tunnel exit site showing the proteins and rRNA surrounding that region.

306

307 To further examine the lower part of the tunnel, we prepared an accurate secondary structure
308 diagram of the mt-rRNA based on the model coordinates (Supplementary Fig. 6). This was
309 important because the sequence diverges substantially and therefore its alignment is not
310 informative. The comparative analysis of the secondary structure diagrams showed that the 50-
311 nucleotide long reduction of rRNA H24, which was reported to have ignited the remodeling of the
312 tunnel path in the *S. cerevisiae* mitoribosome is also observed in our study (Supplementary Fig.
313 15). This prompted us to analyze the region of the tunnel path that was shown to involve structural
314 adaptations in *S. cerevisiae.* While the rRNA occupying this region is generally conserved, proteins
315 uL22m and uL24m are extended in their N-termini so that two helical elements prevent
316 accessibility (Supplementary Fig. 14b). Therefore, the yeast-like tunnel path is obstructed by the
317 mitoribosomal proteins and is unlikely to be functional.

318 Next, we inspected other remodeling of rRNA in the proximity to the tunnel. We identified a
319 deletion of the 28-nucleotide long rRNA H50 segment ~58 Å from the start of the tunnel (Fig. 4c
320 and Supplementary Fig. 15). This remodeling gives rise to a new prominent channel that reaches
321 the mitoribosomal surface ~30 Å away from the original tunnel. The 47-ES1 of the rRNA domain
322 III and the proteins uL22m, uL23m, uL24m, and mL67 shape the boundaries of the tunnel exit
323 leading to the mitoribosomal surface (Fig. 4d). Unlike the bacterial-like tunnel, it forms a wide path
324 that would allow a higher degree of conformational sampling for a synthesized protein.

325 The exit site of this newly identified path is further accompanied with specific structural
326 rearrangements. The rRNA element H59 was deleted, and H53 is unstructured and displaced, which
327 is complemented by acquisition of the mitochondria-specific protein mL67/Mhr1. This
328 mitoribosomal protein is also known as mitochondrial recombinase[24] that mediates mtDNA
329 replication[25] and repair[26]. It has a flexible extension of 25 residues, which is not present in *S.*
330 *cerevisiae*, adjacent to the exit site and pointing towards the membrane plane (Supplementary Fig.
331 14c and 16). Further, mitochondria-specific rRNA expansion segment 96-ES1 also points towards
332 the membrane and the terminal 39 nucleotides appear to be disordered in our map. Together, the
333 data suggest a potential adaptation of the tunnel exit (Supplementary Fig. 14c).

334 From the evolutionary perspective, the internal changes that have led to the deviation of the tunnel
335 path are intrinsic to the rRNA fold. As in the case of the *S. cerevisiae* mitoribosome, the path was
336 altered as a result of a deletion in rRNA. Since rRNA is encoded in the mitochondrial genome, it
337 is the loss of genetic material from mitochondria that leads to a considerable effect on the
338 mitoribosomal structure in the exit tunnel. This determines the geometry of the lower tunnel, which
339 is reflected in the protein folding[21]. Therefore, a further adaptation is required by the means of
340 added protein (mL67/Mhr1) and rRNA (96-ES1) that gain function for the adjustment of the new
341 exit site in respect to the membrane. Consequently, our structure suggests that constructive neutral
342 evolution of mitochondrial DNA[27] drives the architecture of the mitoribosomal exit tunnel.
343 Furthermore, since both mitoribosomes synthesize a similar subset of proteins by employing
344 different exit tunnels, specific characteristics of the mRNA subjected to translation probably do not
345 provide the main factor in the design of the tunnel. Thus, the structural data provides evidence that

346 the functional adaptation, which results in a more proteinaceous exit allowing conformation
347 sampling and nascent polypeptide accessibility, is driven by the rapidly changing mitochondrial
348 DNA.
349

350 **Visualization of mtLSU-Atp25 assembly intermediate suggests a regulatory mechanism**

351 During 3D classification, we recognized a minor population of the particles corresponding to the
352 isolated mtLSU, and subsequent processing resulted in 3.03 Å resolution reconstruction from
353 24,142 particles (Supplementary Fig. 5). Fitting the mtLSU model revealed an extra density that
354 appears as a protein element forming a heterodimer with uL14m. In addition, rRNA at the interface
355 (38-ES2, H63, H67-71, H80, 82-ES6, H101, PTC) appears as unfolded (Fig. 5). Further, the L1
356 stalk changes to a conformation that is more flexible and the density for bL9m next to L1 stalk is
357 absent, whereas all the other mtLSU proteins are present (Fig. 5).

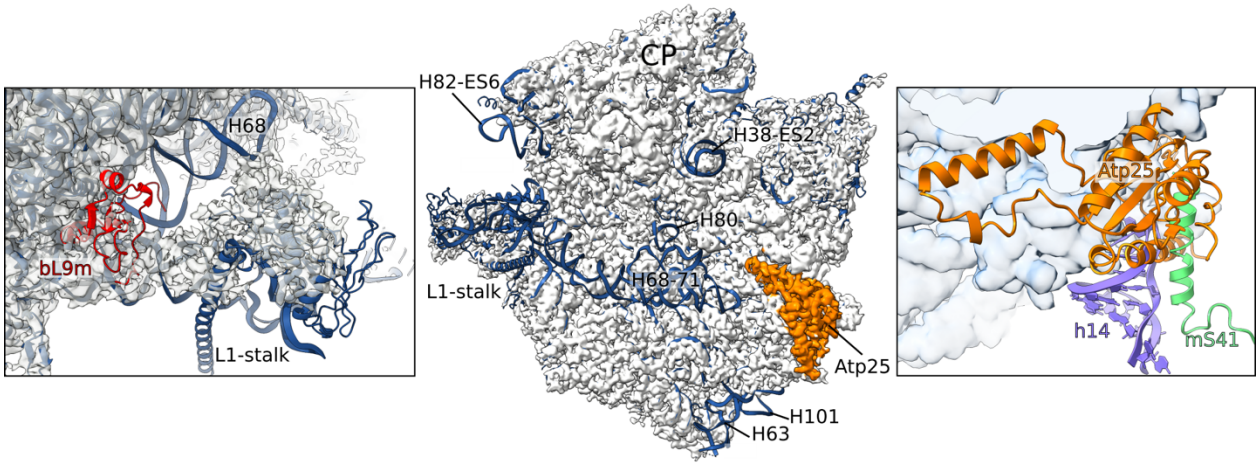


358
359 **Figure 5: Structure and function of the mtLSU-Atp25 assembly complex.** Superposition of the
360 assembly intermediate cryo-EM map (gray) with the mature mtLSU model (blue) reveals unfolded
361 interfacial rRNA, conformational change of the L1 stalk (left panel), missing bL9m (red), presence
362 of Atp25 (orange) that would clash with the mtSSU h14 and mS41, preventing subunit association.
363

364 We identified the extra density as Atp25, an ortholog of the bacterial ribosome silencing factor
365 (Rsf), for which there is no high-resolution structural information in complex with a ribosome[28,29].
366 Its human mitochondrial counterpart, MALSU1, has been shown to involve late assembly
367 stages[13,30]. The gene *Atp25* codes for 699 amino acids, including the targeting sequence, an N-
368 terminal part related to Rsf/MALSU1, and a C-terminal part called the M-domain. In *S. cerevisiae*,
369 ATP25 is cleaved between the N- and C-terminal parts during mitochondrial import[31] and the M-
370 domain forms a separate functional protein that stabilizes the mRNA of the ATP synthase subunit
371 Atp9p[32]. The gene fusion is suggested to have evolved in order to prevent off target effects of
372 Atp25 on the cytosolic ribosomes prior to entry to the mitochondria[31]. We observe only the
373 Rsf/MALSU1-related part of Atp25 on the mitoribosome, confirming the function in the assembly
374 of the mtLSU.

375 Visualization of the mtLSU-Atp25 complex provides a structural basis for the assembly pathway
376 and insight in to possible regulation of translation in mitochondria. Atp25 presents only in the class
377 with the missing bL9m and unfolded interfacial rRNA that affects the L1 stalk. In the mature
378 mitoribosome, bL9m is anchored at the base of the L1 stalk near the E-site, which is stabilized
379 through tertiary interactions with the rRNA. Therefore, the recruitment of bL9m requires specific
380 L1 stalk conformation that is interdependent with rRNA folding, including the PTC. Indeed,
381 ribosomes purified from a bL9-deficient strain of *E. coli* show increased susceptibility to
382 aminoglycosides[33], and the folding of the PTC is among the last maturation events[34,35].
383 Furthermore, bacterial ribosomes lacking bL9 exhibit increased frameshifting[36-38], for which the
384 molecular mechanism has been proposed recently through transiently stalled compacted
385 ribosomes[39].

386 Atp25 bound to uL14m sterically obstructs the binding of the mtSSU by preventing the formation
387 of bridge B8 with its globular domain (Fig. 5). The steric block spans ~25 Å and would clash with
388 h14 of rRNA and the N-terminus of mS26 of the mtSSU. Therefore, the eviction of Atp25 must
389 take place during the final stages of maturation to alleviate the steric hindrance on subunit joining.
390 A similar mechanism was proposed for eIF6 in the cytoplasmic translation apparatus, where protein
391 factor SBDS senses the structural integrity of the functional sites before the displacement[40]. Our
392 data imply that since this is a prerequisite step for the folding of interfacial mt-rRNA into a native-
393 like conformation, it is also a requirement for the binding of bL9m. This shows that bL9m
394 attachment is mechanistically regulated during the assembly of the mitoribosome. Since bL9
395 suppresses frameshifting in bacteria, the structure of the mtLSU-Atp25 lacking bL9m suggests
396 regulation of frameshifting in mitochondrial translation, which might be important for fidelity and
397 reflects an adaptation to the mitochondrial mRNAs.

398

399 **Conclusions**

400 This study reports the first complete model of the translating mitoribosome. It reveals a dedicated
401 mitoribosomal platform for mRNA loading and a newly identified protein mL108 that is associated
402 with the L1 stalk and involved in tRNA translocation. These specific structural features explain the
403 mechanism of translation in mitochondria. The distinct exit tunnel suggests that the evolution of
404 the nascent chain emergence in mitochondria is driven primarily by changes in the rRNA that is
405 encoded in the mitochondrial genome in all species. Finally, the newly described assembly
406 intermediate lacking bL9m proposes a regulatory mechanism for frameshifting.

407

408

409

410

411

412

413

414 # Methods

415 **Purification of mitoribosomes**

416 Mitochondria were isolated from *Neurospora crassa* strain K5-15-23-1[41] which contains a His-
417 tagged version of Oxa1. The *N. crassa* mycelia were grown in aerobic conditions using 10 L of the
418 Vogel's growth medium[42], supplemented with L-lysine and L-leucine at 25°C for 16 h. Each
419 growth flask was supplemented with 0.1% chloramphenicol 1 h prior to harvesting. To separate
420 the moisture from the mycelia, the culture was filtered through muslin. The dry mycelia were
421 transferred to a pre-cooled mortar and pestle to lyse the cells. All further operations were performed
422 at 4°C. The cells were lysed using sea-sand (silicon dioxide) and SEMP buffer (250 mM sucrose,
423 1 mM ethylenediaminetetraacetic acid (EDTA), 10 mM MOPS-KOH pH 7.2, 2 mM
424 phenylmethanesulfonyl fluoride (PMSF), and 0.2% chloramphenicol), by applying a 20 min
425 grinding course. Sand and cell debris were removed using differential centrifugation at low-speed
426 (2000 x g). A subsequent high-speed centrifugation step (17,500 x g) was carried out to sediment
427 crude mitochondria. The mitochondrial pellet was then resuspended in SEM buffer (250 mM
428 sucrose, 1 mM EDTA, and 10 mM MOPS-KOH pH 7.2). To further purify, the crude mitochondria
429 were undergone a sucrose gradient in SEM buffer for 1h at 28,000 rpm with an SW40 Ti rotor
430 (Beckman Coulter). Mitochondrial band was pooled and stored at -80 °C.

431 Mitochondria were lysed in 4 volumes of lysis buffer (25 mM Hepes-KOH pH 7.5, 20 mM KCl,
432 15 mM $Mg(OAc)_2$, 2% *n*-dodecyl-β-D-maltoside (DDM), 0.0075 % cardiolipin, 2 mM
433 dithiothreitol (DTT), 1 tablet of protease inhibitor (cOmplete™, Roche), and RNase inhibitor
434 (RNaseOUT, Invitrogen)) and incubated for 5 min at 4°C. The membrane was separated by
435 centrifugation of the mitochondrial lysate at 30,000 x g for 20 min followed by a second
436 centrifugation step with the same settings. The supernatant was loaded onto a 1.0 M sucrose
437 cushion in the resuspension buffer (20 mM Hepes-KOH pH 7.5, 15 mM KCL, 15 mM $Mg(OAc)_2$,
438 0.05% DDM, 0.0075% cardiolipin, and 2 mM DTT) with RNase inhibitor and centrifuged at
439 48,000 rpm with a 70 Ti rotor for 4 h. The pellet was then resuspended in the resuspension buffer,
440 loaded on a 15-30% sucrose gradient in the resuspension buffer, and centrifuged at 23,000 rpm
441 with an SW40 Ti for 16 h at 4°C. Fractions containing mitoribosomes were collected and the
442 mitorobosomes were pelleted by centrifugation at 100,000 rpm with a TLA120.2 rotor (Beckman
443 Coulter) for 45 min at 4°C and resuspended in the resuspension buffer.

444

445 **Cryo-EM and image processing**

446 Freshly purified mitorobosome sample ($A_{260}$ = 3.0) was used for grid preparation. 3 µl aliquots of
447 purified mitoribsomes was incubated for 30 s on glow-discharged holey carbon grids (Quantifoil
448 R2/2, 300 mesh, copper) pre-coated with a home-made continuous carbon film with thickness of ~
449 27 Å. The grids were thereafter vitrified in a liquid ethane with a Vitrobot MKIV (FEI/Thermo
450 Fisher) using a blotting time of 3 s at 4°C and 100% humidity. Micrographs were collected with a
451 300 kV Titan Krios (FEI/Thermo Fisher) transmission electron microscope, 70 µm C2 aperture,
452 using a slit width of 20 eV on a GIF-Quantum energy filter (Gatan). A K2 summit detector
453 (GATAN) was used in the counting mode at the calibrated magnification of 130,000 (yielding a

454 pixel size of 1.06 Å). An exposure time of 9 s yielding a total of 35 e/Å$^2$ was dose fractionated into
455 20 frames. In total 3,172 movies were collected automatically during two consecutive days using
456 EPU (FEI/Thermo Fisher) data collection software. Defocus values ranged between 0.8 and 3.0
457 μm.

458 Collected movie frames were aligned and corrected for both global and non-uniform local beam-
459 induced movements using MotionCor[43] and the contrast transfer function (CTF) parameters were
460 estimated using Gctf[44], inside the SCIPION program[45]. Subsequent data processing steps were
461 performed using RELION-2.1 and 3.0[46]. First, 647 particles were manually picked, followed by
462 two-dimensional (2D) classification. Four good 2D class averages were used for reference-based
463 picking for the second round. 265,710 picked particles were subjected to 2D classification and 50
464 good 2D classes were selected (Figure S1). Retained 223,605 particles were classified into six
465 classes by three-dimensional (3D) classification, resulted in four good mito-monosome classes
466 (131,806 particles), one class with weak mtSSU density (36,053 particles), and one low quality
467 class containing junks. From the class with weak mtSSU density, isolated mtLSU particles (24,142
468 particles) are classified out by further 3D classification.

469 Pooled good particles were subjected to 3D auto-refinement. Per-particle CTF refinement[47],
470 followed by Bayesian polishing[48] and the second round of per particle CTF refinement to improve
471 resolution, resulted in reconstructions of mito-monosome and the isolated mtLSU with 2.83 and
472 3.03 Å resolution, respectively (Figure S1). Resolution is estimated based on the gold standard
473 criterion of Fourier shell correlation (FSC) = 0.143 between the reconstructed two half maps.

474 Due to the relative movement between the mtSSU and mtLSU in monosome, we suffered from low
475 resolution in the mtSSU. We therefore decided to improve the quality of the maps by focused
476 masked refinement for the mtSSU and mtLSU separately. We obtained the masked maps of mtLSU
477 and mtSSU with 2.74 and 2.85 Å resolution, respectively. Further, improvement of local
478 resolutions was achieved by focused refinement using the local masks as described in the
479 Supplementary Material.

480 All the density maps were locally resolution filtered by applying a negative B-factor estimated
481 automatically by RELION-3.0.

482 The observed motion between mtLSU and mtSSU prompted us to separate possible sub-states of
483 the monosome. Firstly, we classified the particles in two major classes (ratcheted and non-
484 ratcheted states) by overall 3D classification. To facilitate classifying tRNA states, signal
485 subtraction of ribosome was performed using a cylindrical mask covering the A-, P-, and E-sites
486 for the ratcheted and non-ratcheted states separately by RELION 3.0, following by focused 3D
487 classification without alignment. For the ratcheted state, the same cylindrical mask was applied
488 for the classification, which separated the P/E hybrid tRNA bound mitoribosomes (37,908
489 particles). For non-ratcheted state, smaller masks were needed to classify tRNAs. The P/P tRNA
490 bound mitoribosomes were separated applying a mask covering only the P-site, while E/E tRNA
491 bound ones were separated by a mask covering only the E-site. The P/P tRNA and E/E tRNA
492 bound mitoribosomes were 24,611 and 23,802 particles, respectively. Among them, only 4,136
493 particles are overlapping and have both P/P and E/E tRNAs, which are too few for high-

resolution reconstruction. Local resolution of the tRNA bound mitoribosomes were also improved by using local masked refinement as described in the Supplementary Material.

**Model building and refinement**

Model building was carried out in Coot[49]. Rigid body docking was carried out in UCSF Chimera[50]. The model of the *S. cerevisiae* mitoribosome (PDB ID: 5MRC) was used as a reference. For proteins whose orthologs existed in *S. cerevisiae* structure, the homology models of *N. crassa* were generated by SWISS Model[51], placed into the density, manually revised and built unmodeled and unique regions, and real space fit in Coot. Previously unknown or unmodeled proteins were modeled *de novo* in Coot. For the correct assignment of the proteins, sequence stretches of reasonable quality were directly identified from the map and then applied to BLAST[52] and/or compared to the protein sequences gained from mass spectrometry (Supplementary Table 4). The ribosomal protein mL108 was named according to the standard nomenclature widely accepted in the ribosome community[53]. The number was chosen in a chronological order of discover also considering unpublished data. The entire rRNAs, tRNAs, and mRNAs were modeled *de novo* in Coot. Since bound tRNAs and mRNAs are mixture of any mitochondrial ones, each residue was assigned as either A, U, G, or C, based on the density and conservation. Ligands and metal ions were placed into the density.

For model refinement of the consensus mtLSU and mtSSU and the monosomes in the three tRNA states, the local masked refined maps with B-factor sharpening and local-resolution filtering were merged using the program phenix_combine_focused_maps in the Phenix software suite[54], thereby generating a map for model refinement. For the isolated mtLSU, the overall refined map with B-factor sharpening and local-resolution filtering was used for model refinement. Refinement of all models was performed using Phenix.rel_space_refine[55]. The final structure was validated using the MolProbity[56] implementation of the Phenix suite.

**Figure preparation**

All structural figures were generated with PyMOL[57], UCSF Chimera[50], and ChimeraX[58]. The secondary structure diagrams of the 16S and 23S rRNA were generated using XRNA (http://rna.ucsc.edu/rnacenter/xrna/xrna.html).The shape of the polypeptide tunnels were calculated with the software Mole[59].

**Data availability**

Cryo-EM maps have been deposited at the EMDB with the following accession codes: EMD-10958, EMD-10961, EMD-10962, EMD-10963, EMD-10965, EMD-10966, EMD-10967, EMD-10968, EMD-10969, EMD-10970, EMD-10971, EMD-10972 EMD-10973, EMD-10974, EMD-10975, EMD-10976, EMD-10977, EMD-10978, EMD-10979, EMD-10980, EMD-10981, EMD-10982, EMD-10983, EMD-10984, EMD-10985, EMD-10986, EMD-10988, EMD-10989, EMD-10990, EMD-10991 and EMD-10992. The atomic coordinates have been deposited at the PDB with the following accession codes: 6YWS, 6YW5, 6YWX, 6YWY, 6YWE and 6YWV.

534 **References**


535 1 Brown, A. *et al.* Structure of the large ribosomal subunit from human mitochondria. *Science*
536 **346**, 718-722, doi:10.1126/science.1258026 (2014).
537 2 Amunts, A., Brown, A., Toots, J., Scheres, S. H. W. & Ramakrishnan, V. Ribosome. The
538 structure of the human mitochondrial ribosome. *Science* **348**, 95-98,
539 doi:10.1126/science.aaa1193 (2015).
540 3 Greber, B. J. *et al.* Architecture of the large subunit of the mammalian mitochondrial
541 ribosome. *Nature* **505**, 515-519, doi:10.1038/nature12890 (2014).
542 4 Greber, B. J. *et al.* Ribosome. The complete structure of the 55S mammalian mitochondrial
543 ribosome. *Science* **348**, 303-308, doi:10.1126/science.aaa3872 (2015).
544 5 Amunts, A. *et al.* Structure of the yeast mitochondrial large ribosomal subunit. *Science* **343**,
545 1485-1489, doi:10.1126/science.1249410 (2014).
546 6 Desai, N., Brown, A., Amunts, A. & Ramakrishnan, V. The structure of the yeast
547 mitochondrial ribosome. *Science* **355**, 528-531, doi:10.1126/science.aal2415 (2017).
548 7 van der Sluis, E. O. *et al.* Parallel Structural Evolution of Mitochondrial Ribosomes and
549 OXPHOS Complexes. *Genome Biol Evol* **7**, 1235-1251, doi:10.1093/gbe/evv061 (2015).
550 8 Kuntzel, H. & Noll, H. Mitochondrial and cytoplasmic polysomes from Neurospora crassa.
551 *Nature* **215**, 1340-1345, doi:10.1038/2151340a0 (1967).
552 9 Kuntzel, H. Mitochondrial and cytoplasmic ribosomes from Neurospora crassa:
553 characterization of their subunits. *J Mol Biol* **40**, 315-320, doi:10.1016/0022-
554 2836(69)90481-1 (1969).
555 10 Neupert, W., Sebald, W., Schwab, A. J., Massinger, P. & Bucher, T. Incorporation in vivo
556 of 14C-labelled amino acids into the proteins of mitochondrial ribosomes from Neurospora
557 crassa sensitive to cycloheximide and insensitive to Chloramphenicol. *Eur J Biochem* **10**,
558 589-591, doi:10.1111/j.1432-1033.1969.tb00730.x (1969).
559 11 Nargang, F. E., Preuss, M., Neupert, W. & Herrmann, J. M. The Oxa1 protein forms a
560 homooligomeric complex and is an essential part of the mitochondrial export translocase in
561 Neurospora crassa. *J Biol Chem* **277**, 12846-12853, doi:10.1074/jbc.M112099200 (2002).
562 12 Aibara, S., Andrell, J., Singh, V. & Amunts, A. Rapid Isolation of the Mitoribosome from
563 HEK Cells. *J Vis Exp*, doi:10.3791/57877 (2018).
564 13 Brown, A. *et al.* Structures of the human mitochondrial ribosome in native states of
565 assembly. *Nat Struct Mol Biol* **24**, 866-869, doi:10.1038/nsmb.3464 (2017).
566 14 Kim, H. J., Maiti, P. & Barrientos, A. Mitochondrial ribosomes in cancer. *Semin Cancer*
567 *Biol* **47**, 67-81, doi:10.1016/j.semcancer.2017.04.004 (2017).
568 15 Robinson, G. C. *et al.* The structure of F(1)-ATPase from Saccharomyces cerevisiae
569 inhibited by its regulatory protein IF(1). *Open Biol* **3**, 120164, doi:10.1098/rsob.120164
570 (2013).
571 16 Cabezon, E., Montgomery, M. G., Leslie, A. G. & Walker, J. E. The structure of bovine
572 F1-ATPase in complex with its regulatory protein IF1. *Nat Struct Biol* **10**, 744-750,
573 doi:10.1038/nsb966 (2003).
574 17 Cabezon, E., Runswick, M. J., Leslie, A. G. & Walker, J. E. The structure of bovine IF(1),
575 the regulatory subunit of mitochondrial F-ATPase. *EMBO J* **20**, 6990-6996,
576 doi:10.1093/emboj/20.24.6990 (2001).
577 18 Petrov, A. S. *et al.* Structural Patching Fosters Divergence of Mitochondrial Ribosomes.
578 *Mol Biol Evol* **36**, 207-219, doi:10.1093/molbev/msy221 (2019).

579 19 Qu, X., Lancaster, L., Noller, H. F., Bustamante, C. & Tinoco, I., Jr. Ribosomal protein S1
580 unwinds double-stranded RNA in multiple steps. *Proc Natl Acad Sci U S A* **109**, 14458-
581 14463, doi:10.1073/pnas.1208950109 (2012).
582 20 Komoda, T. *et al.* The A-site finger in 23 S rRNA acts as a functional attenuator for
583 translocation. *J Biol Chem* **281**, 32303-32309, doi:10.1074/jbc.M607058200 (2006).
584 21 Kudva, R. *et al.* The shape of the bacterial ribosome exit tunnel affects cotranslational
585 protein folding. *Elife* **7**, doi:10.7554/eLife.36326 (2018).
586 22 Dao Duc, K., Batra, S. S., Bhattacharya, N., Cate, J. H. D. & Song, Y. S. Differences in the
587 path to exit the ribosome across the three domains of life. *Nucleic Acids Res* **47**, 4198-4210,
588 doi:10.1093/nar/gkz106 (2019).
589 23 Shanmuganathan, V. *et al.* Structural and mutational analysis of the ribosome-arresting
590 human XBP1u. *Elife* **8**, doi:10.7554/eLife.46267 (2019).
591 24 Ling, F. & Shibata, T. Recombination-dependent mtDNA partitioning: in vivo role of
592 Mhr1p to promote pairing of homologous DNA. *EMBO J* **21**, 4730-4740,
593 doi:10.1093/emboj/cdf466 (2002).
594 25 Ling, F. & Shibata, T. Mhr1p-dependent concatemeric mitochondrial DNA formation for
595 generating yeast mitochondrial homoplasmic cells. *Mol Biol Cell* **15**, 310-322,
596 doi:10.1091/mbc.e03-07-0508 (2004).
597 26 Prasai, K., Robinson, L. C., Scott, R. S., Tatchell, K. & Harrison, L. Evidence for double-
598 strand break mediated mitochondrial DNA replication in Saccharomyces cerevisiae.
599 *Nucleic Acids Res* **45**, 7760-7773, doi:10.1093/nar/gkx443 (2017).
600 27 Stoltzfus, A. Constructive neutral evolution: exploring evolutionary theory's curious
601 disconnect. *Biol Direct* **7**, 35, doi:10.1186/1745-6150-7-35 (2012).
602 28 Hauser, R. *et al.* RsfA (YbeB) proteins are conserved ribosomal silencing factors. *PLoS*
603 *Genet* **8**, e1002815, doi:10.1371/journal.pgen.1002815 (2012).
604 29 Li, X. *et al.* Structure of Ribosomal Silencing Factor Bound to Mycobacterium tuberculosis
605 Ribosome. *Structure* **23**, 2387, doi:10.1016/j.str.2015.11.002 (2015).
606 30 Rorbach, J., Gammage, P. A. & Minczuk, M. C7orf30 is necessary for biogenesis of the
607 large subunit of the mitochondrial ribosome. *Nucleic Acids Res* **40**, 4097-4109,
608 doi:10.1093/nar/gkr1282 (2012).
609 31 Woellhaf, M. W., Sommer, F., Schroda, M. & Herrmann, J. M. Proteomic profiling of the
610 mitochondrial ribosome identifies Atp25 as a composite mitochondrial precursor protein.
611 *Mol Biol Cell* **27**, 3031-3039, doi:10.1091/mbc.E16-07-0513 (2016).
612 32 Zeng, X., Barros, M. H., Shulman, T. & Tzagoloff, A. ATP25, a new nuclear gene of
613 Saccharomyces cerevisiae required for expression and assembly of the Atp9p subunit of
614 mitochondrial ATPase. *Mol Biol Cell* **19**, 1366-1377, doi:10.1091/mbc.E07-08-0746
615 (2008).
616 33 Naganathan, A., Wood, M. P. & Moore, S. D. The large ribosomal subunit protein L9
617 enables the growth of EF-P deficient cells and enhances small subunit maturation. *PLoS*
618 *One* **10**, e0120060, doi:10.1371/journal.pone.0120060 (2015).
619 34 Li, N. *et al.* Cryo-EM structures of the late-stage assembly intermediates of the bacterial
620 50S ribosomal subunit. *Nucleic Acids Res* **41**, 7073-7083, doi:10.1093/nar/gkt423 (2013).
621 35 Jomaa, A. *et al.* Functional domains of the 50S subunit mature late in the assembly process.
622 *Nucleic Acids Res* **42**, 3419-3435, doi:10.1093/nar/gkt1295 (2014).
623 36 Atkins, J. F., Loughran, G., Bhatt, P. R., Firth, A. E. & Baranov, P. V. Ribosomal
624 frameshifting and transcriptional slippage: From genetic steganography and cryptography
625 to adventitious use. *Nucleic Acids Res* **44**, 7007-7078, doi:10.1093/nar/gkw530 (2016).

37 Herr, A. J., Nelson, C. C., Wills, N. M., Gesteland, R. F. & Atkins, J. F. Analysis of the roles of tRNA structure, ribosomal protein L9, and the bacteriophage T4 gene 60 bypassing signals during ribosome slippage on mRNA. *J Mol Biol* **309**, 1029-1048, doi:10.1006/jmbi.2001.4717 (2001).

38 Seidman, J. S., Janssen, B. D. & Hayes, C. S. Alternative fates of paused ribosomes during translation termination. *J Biol Chem* **286**, 31105-31112, doi:10.1074/jbc.M111.268201 (2011).

39 Smith, A. M., Costello, M. S., Kettring, A. H., Wingo, R. J. & Moore, S. D. Ribosome collisions alter frameshifting at translational reprogramming motifs in bacterial mRNAs. *Proc Natl Acad Sci U S A* **116**, 21769-21779, doi:10.1073/pnas.1910613116 (2019).

40 Weis, F. *et al.* Mechanism of eIF6 release from the nascent 60S ribosomal subunit. *Nat Struct Mol Biol* **22**, 914-919, doi:10.1038/nsmb.3112 (2015).

41 Funes, S., Nargang, F. E., Neupert, W. & Herrmann, J. M. The Oxa2 protein of Neurospora crassa plays a critical role in the biogenesis of cytochrome oxidase and defines a ubiquitous subbranch of the Oxa1/YidC/Alb3 protein family. *Mol Biol Cell* **15**, 1853-1861, doi:10.1091/mbc.e03-11-0789 (2004).

42 Vogel, H. J. A convenient growth medium for Neurospora crassa. *Microbial Genet Bull.* **13**, 42-43 (1956).

43 Li, X. *et al.* Electron counting and beam-induced motion correction enable near-atomic-resolution single-particle cryo-EM. *Nat Methods* **10**, 584-590, doi:10.1038/nmeth.2472 (2013).

44 Zhang, K. Gctf: Real-time CTF determination and correction. *J Struct Biol* **193**, 1-12, doi:10.1016/j.jsb.2015.11.003 (2016).

45 de la Rosa-Trevin, J. M. *et al.* Scipion: A software framework toward integration, reproducibility and validation in 3D electron microscopy. *J Struct Biol* **195**, 93-99, doi:10.1016/j.jsb.2016.04.010 (2016).

46 Kimanius, D., Forsberg, B. O., Scheres, S. H. & Lindahl, E. Accelerated cryo-EM structure determination with parallelisation using GPUs in RELION-2. *Elife* **5**, doi:10.7554/eLife.18722 (2016).

47 Zivanov, J. *et al.* New tools for automated high-resolution cryo-EM structure determination in RELION-3. *Elife* **7**, doi:10.7554/eLife.42166 (2018).

48 Zivanov, J., Nakane, T. & Scheres, S. H. W. A Bayesian approach to beam-induced motion correction in cryo-EM single-particle analysis. *IUCrJ* **6**, 5-17, doi:10.1107/S205225251801463X (2019).

49 Emsley, P. & Cowtan, K. Coot: model-building tools for molecular graphics. *Acta Crystallogr D Biol Crystallogr* **60**, 2126-2132, doi:10.1107/S0907444904019158 (2004).

50 Pettersen, E. F. *et al.* UCSF Chimera--a visualization system for exploratory research and analysis. *J Comput Chem* **25**, 1605-1612, doi:10.1002/jcc.20084 (2004).

51 Waterhouse, A. *et al.* SWISS-MODEL: homology modelling of protein structures and complexes. *Nucleic Acids Res* **46**, W296-W303, doi:10.1093/nar/gky427 (2018).

52 Altschul, S. F., Gish, W., Miller, W., Myers, E. W. & Lipman, D. J. Basic local alignment search tool. *J Mol Biol* **215**, 403-410, doi:10.1016/S0022-2836(05)80360-2 (1990).

53 Ban, N. *et al.* A new system for naming ribosomal proteins. *Curr Opin Struct Biol* **24**, 165-169, doi:10.1016/j.sbi.2014.01.002 (2014).

54 Liebschner, D. *et al.* Macromolecular structure determination using X-rays, neutrons and electrons: recent developments in Phenix. *Acta Crystallogr D Struct Biol* **75**, 861-877, doi:10.1107/S2059798319011471 (2019).

673 55 Afonine, P. V. *et al.* Real-space refinement in PHENIX for cryo-EM and crystallography.
674 *Acta Crystallogr D Struct Biol* **74**, 531-544, doi:10.1107/S2059798318006551 (2018).
675 56 Williams, C. J. *et al.* MolProbity: More and better reference data for improved all-atom
676 structure validation. *Protein Sci* **27**, 293-315, doi:10.1002/pro.3330 (2018).
677 57 DeLano, W. L. Pymol: An open-source molecular graphics tool. . *CCP4 Newsletter On*
678 *Protein Crystallography* **40**, 82-92 (2002).
679 58 Goddard, T. D. *et al.* UCSF ChimeraX: Meeting modern challenges in visualization and
680 analysis. *Protein Sci* **27**, 14-25, doi:10.1002/pro.3235 (2018).
681 59 Pravda, L. *et al.* MOLEonline: a web-based tool for analyzing channels, tunnels and pores
682 (2018 update). *Nucleic Acids Res* **46**, W368-W373, doi:10.1093/nar/gky309 (2018).
683 60 Bason, J. V., Montgomery, M. G., Leslie, A. G. & Walker, J. E. Pathway of binding of the
684 intrinsically disordered mitochondrial inhibitor protein to F1-ATPase. *Proc Natl Acad Sci*
685 *U S A* **111**, 11305-11310, doi:10.1073/pnas.1411560111 (2014).

686

687 **Acknowledgements** We thank Frank Nargang for providing the *N. crassa* strain, and Marta
688 Carroni and Julian Conrad for supporting cryo-EM data collection. This work was supported by
689 the Swedish Foundation for Strategic Research (FFL15:0325), Ragnar Söderberg Foundation
690 (M44/16), Swedish Research Council (NT_2015-04107), Cancerfonden (2017/1041), European
691 Research Council (ERC-2018-StG-805230), Knut and Alice Wallenberg Foundation (2018.0080),
692 EMBO Young Investigator Program. Y.I. is supported by H2020-MSCA-IF-2017 (799399-
693 Itohribo). The data was collected at the SciLifeLab cryo-EM facility funded by the Knut and Alice
694 Wallenberg, Family Erling Persson, and Kempe foundations. Mass spectrometry analysis was
695 performed by the clinical proteomics mass spectrometry facility of the Karolinska University
696 Hospital and SciLifeLab proteogenomics core facility. We thank John Walker and Alan Brown for
697 constructive comments.

698

699 **Author contributions** A.A. designed the project. N.M prepared the sample and collected cryo-EM
700 data. Y.I., A.N. and N.M. processed the data and built the model. Y.I., A.N. and A.A. wrote the
701 manuscript with help from N.M. and J.H.

702

703 **Competing interests** The authors declare no competing interests.

704 Supplementary Information for

# 705 Analysis of translating mitoribosome reveals functional 706 characteristics of protein synthesis in mitochondria of fungi

707

708 Yuzuru Itoh[1,2†], Andreas Naschberger[1†], Narges Mortezaei[1†], Johannes Herrmann[3]
709 and Alexey Amunts[1,2]*

710

711 [1]Science for Life Laboratory, Department of Biochemistry and Biophysics, Stockholm
712 University, 17165 Solna, Sweden

713 [2]Department of Medical Biochemistry and Biophysics, Karolinska Institutet, 17165
714 Solna, Sweden

715 [3]Cell Biology, University of Kaiserslautern, Erwin-Schrödinger-Straße 13, 67663 Kaiserslautern,
716 Germany

717 † These authors contributed equally to this work.

718

719

720 *Correspondence and request for material should be addressed to amunts@scilifelab.se

721

722

723 **This file includes:**

724 Supplementary Figures 1-16

725 Supplementary Tables 1-4

## Supplementary Figures

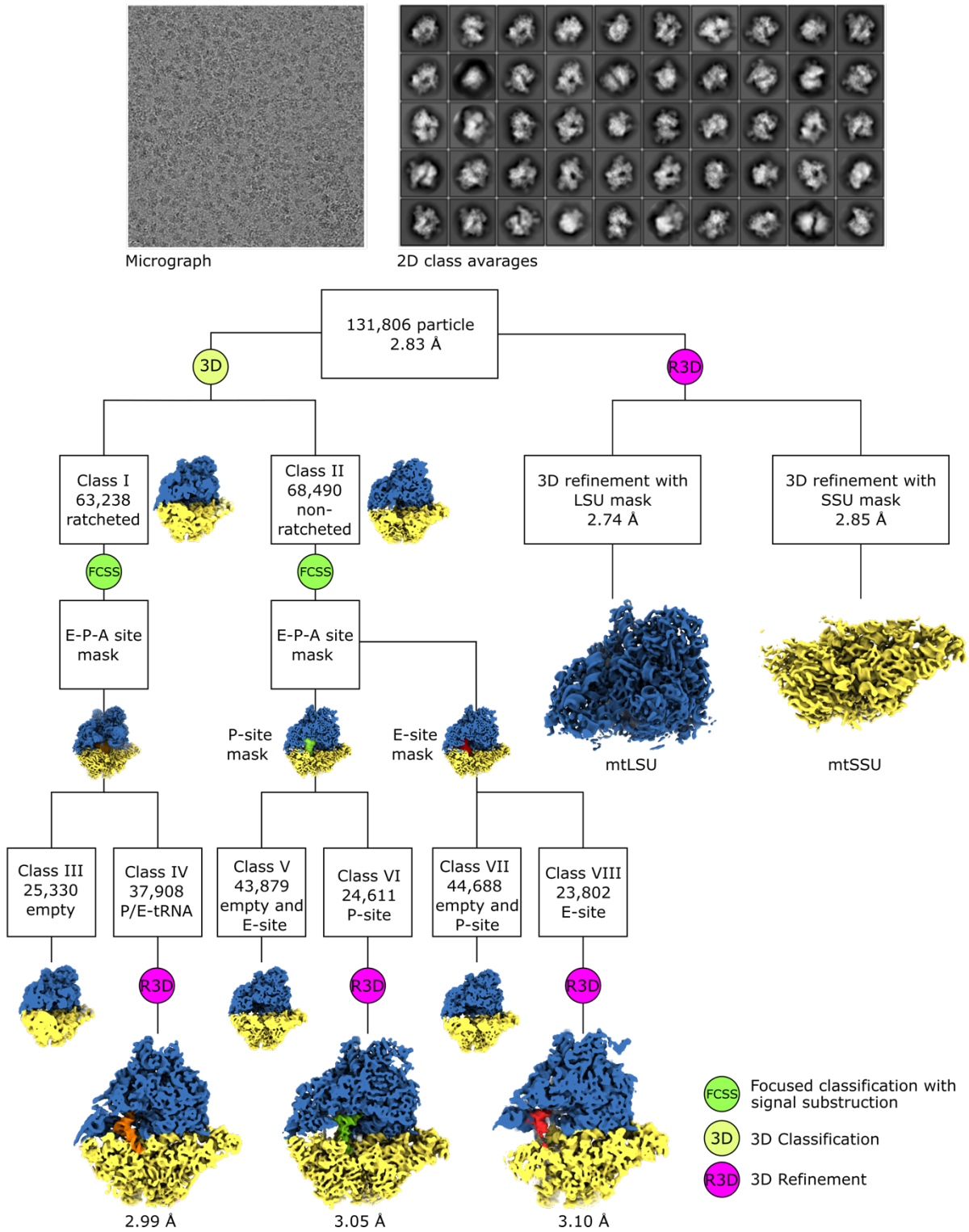


**Supplementary Figure 1. Cryo-EM data collection and processing scheme.** Representative micrograph and 2D class averages. Data refinement protocol and classification scheme for mtLSU, mtSSU and monosome in three tRNA bound states.

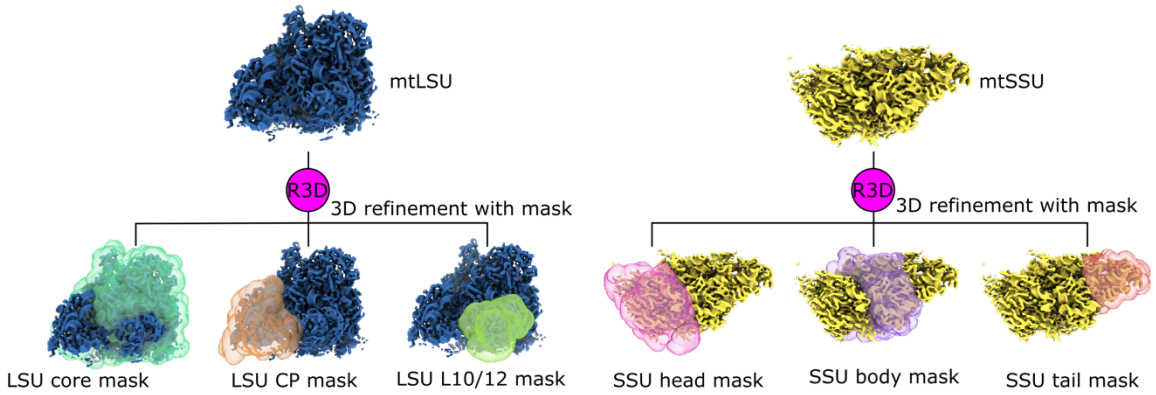


**Supplementary Figure 2. Masked refinement of mitoribosomal subunits.** Masks for mtLSU core, CP, L7/12 stalk; mtSSU head, body, tail were used to improve the density locally.

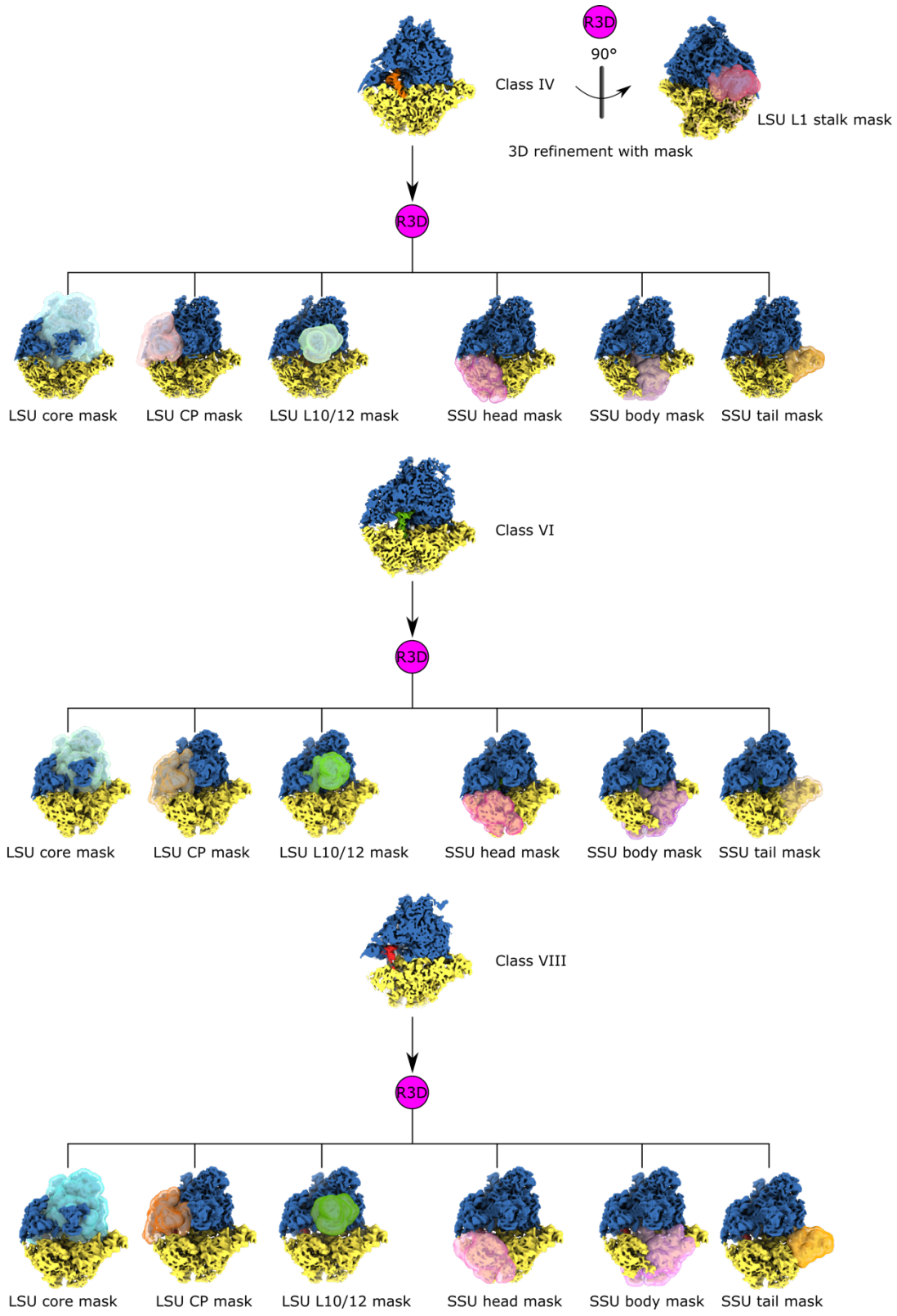


**Supplementary Figure 3. Masking refinement of the mitoribosomes in tRNA bound states.**

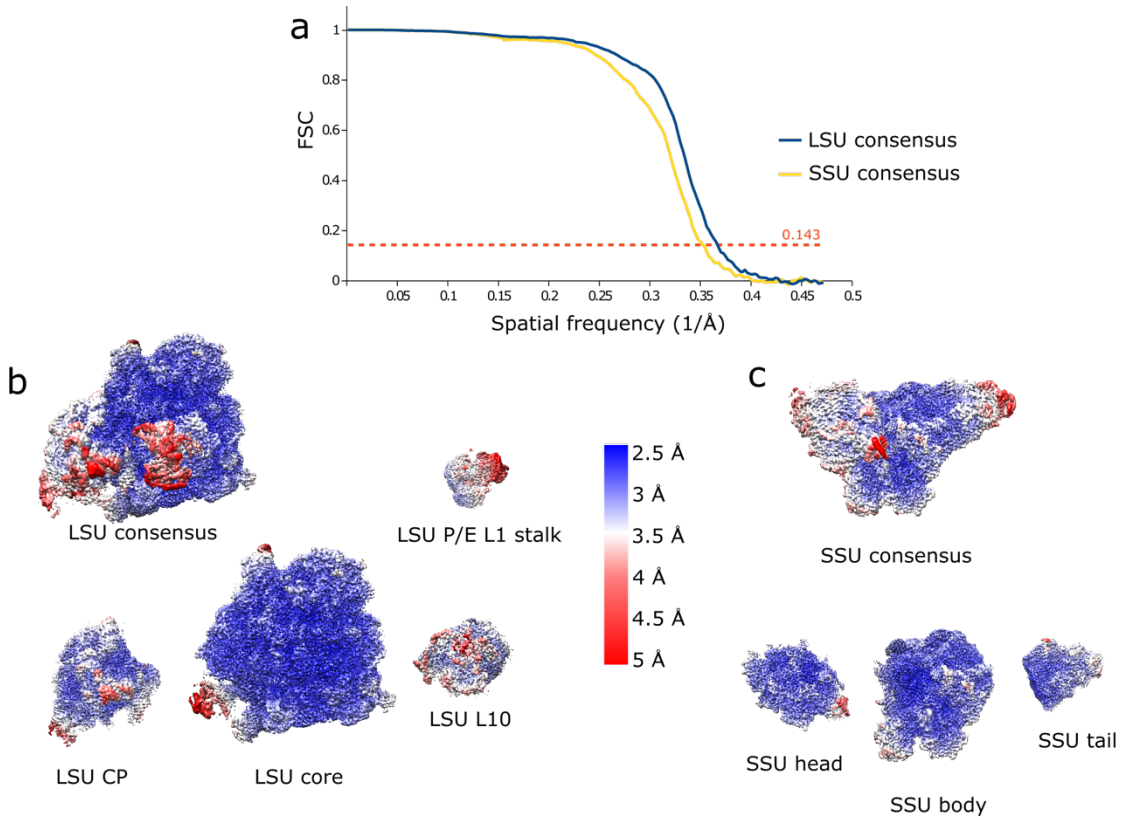


736

737 **Supplementary Figure 4. Overall and local resolution estimations of mitoribosomal subunits.**
738 **a,** Fourier Shell Correlation (FSC) curves for the refined maps of mtLSU and mtSSU. Value of
739 0.143 is indicated. **b,** mtLSU cryo-EM maps viewed according to local resolution. **c,** mtSSU cryo-
740 EM maps viewed according to local resolution.

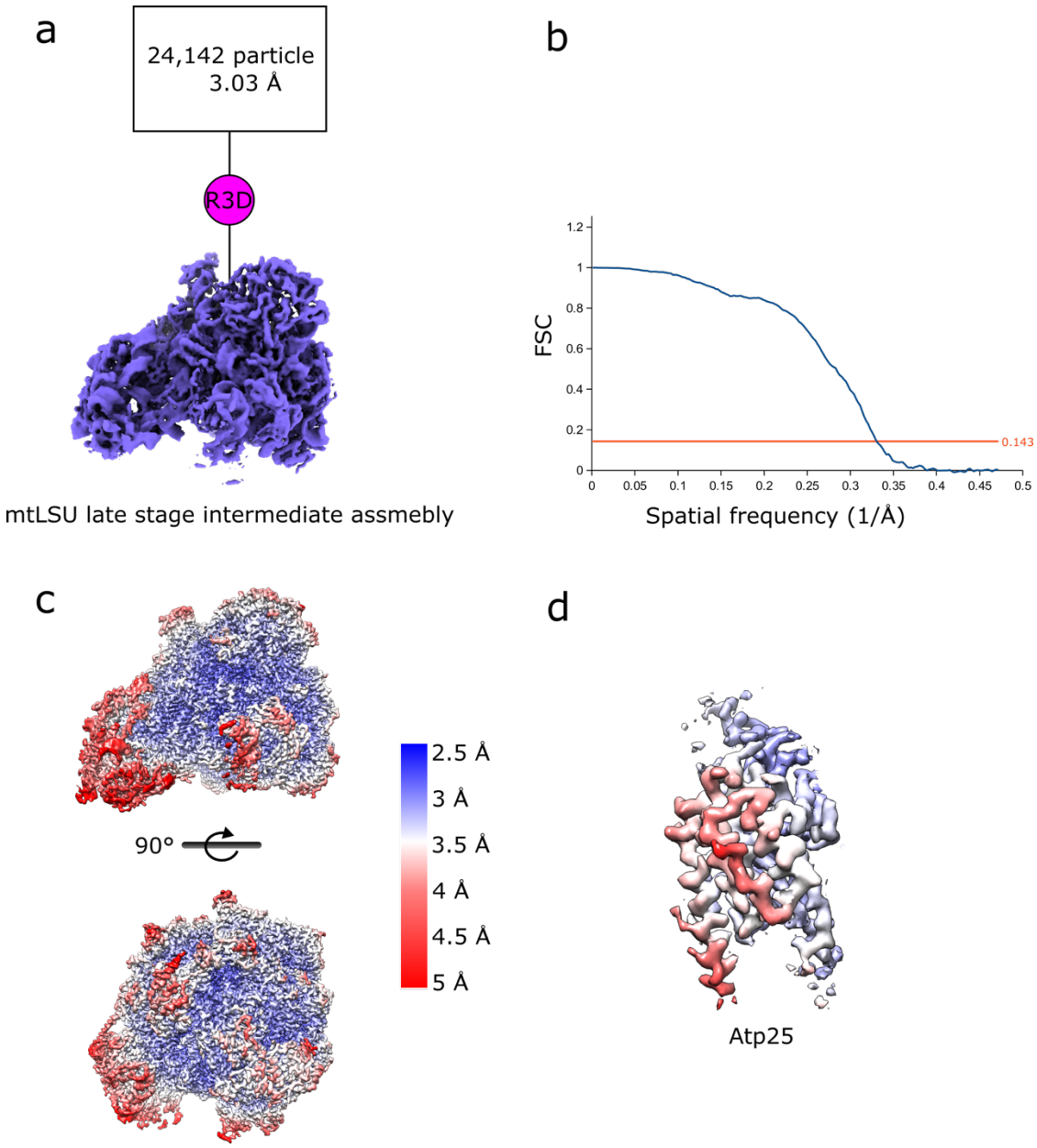


741

742 **Supplementary Figure 5. Data processing and overall and local resolution estimations of**
743 **mtLSU-Atp25 assembly intermediate. a,** Processing scheme. **b,** Fourier Shell Correlation (FSC)
744 curves for the refined map. Gold standard value of 0.143 is indicated. **c,** mtLSU-Atp25 assembly
745 intermediate cryo-EM maps colored according to local resolution. **d,** Zoomed in map for Atp25
746 colored by local resolution.

747

748

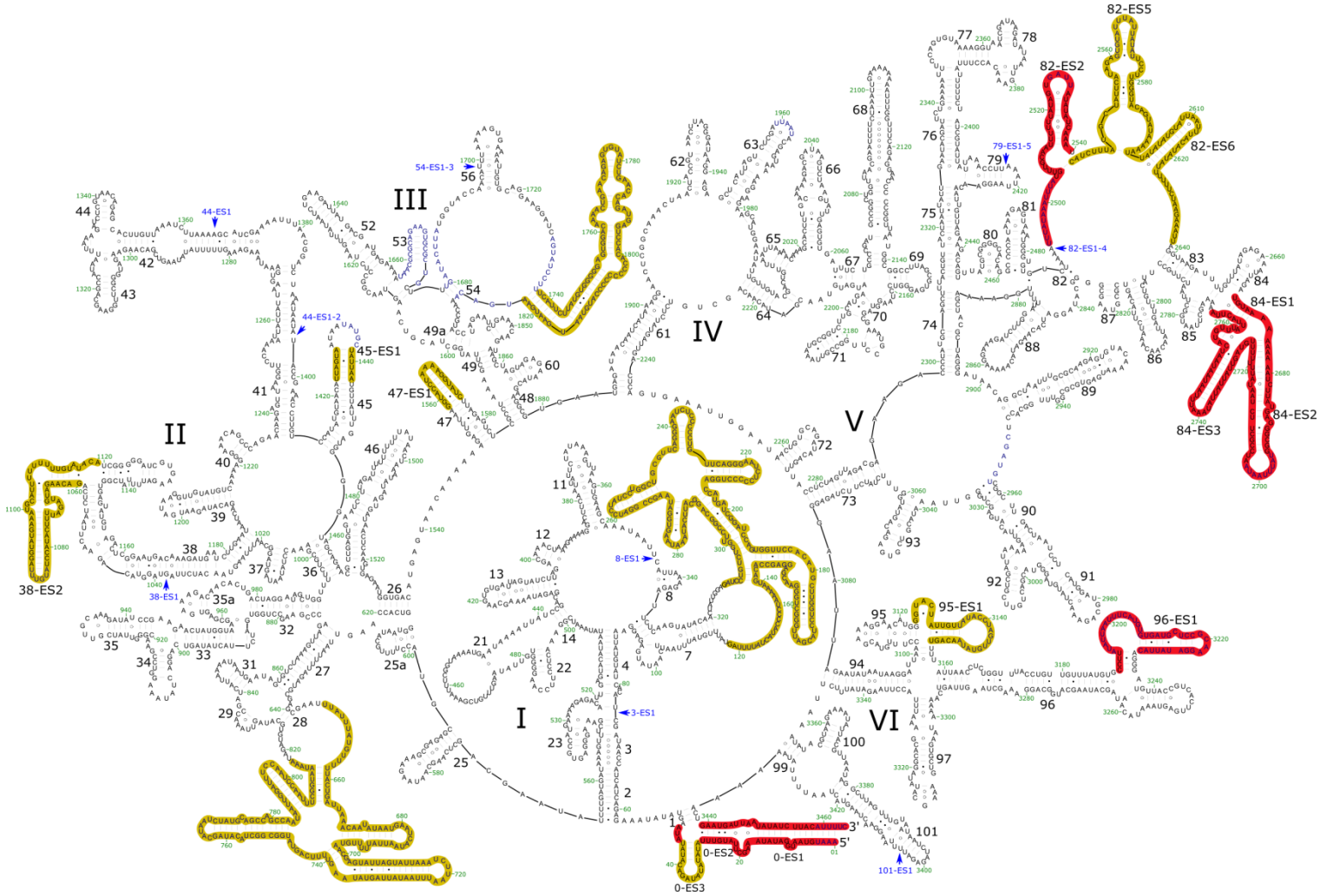


**Supplementary Figure 6. Structure-based secondary structure diagram of the mtLSU rRNA.** Expansion segments shared between *N. crassa* and *S. cerevisiae* are highlighted with red, specific expansion segments are highlighted with yellow. Those present in *S. cerevisiae* only are indicated by light blue arrows. rRNA somains are labeled with roman numerals.

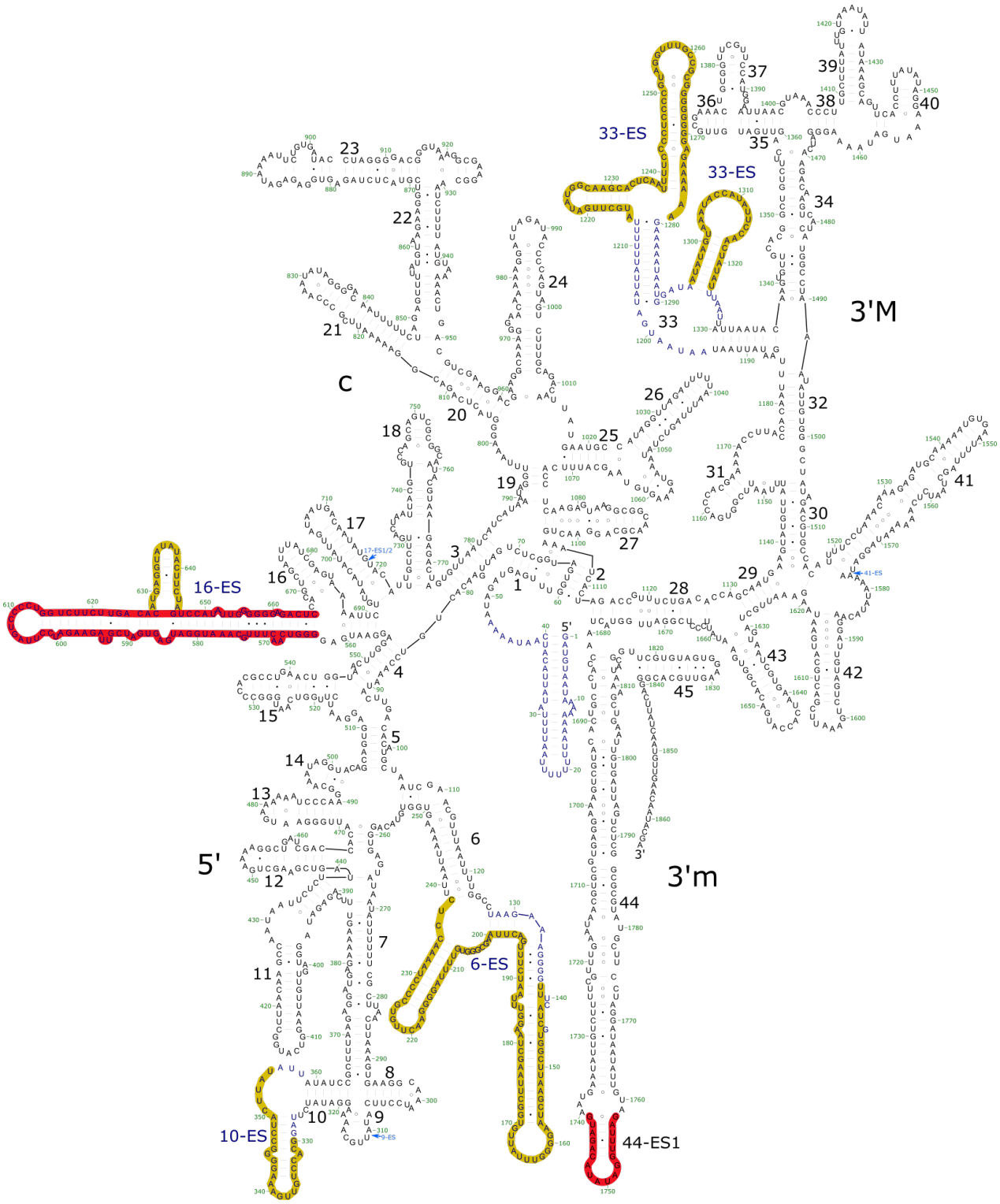


**Supplementary Figure 7. Structure-based secondary structure diagram of the mtLSU rRNA.** Expansion segments shared between *N. crassa* and *S. cerevisiae* are highlighted with red, specific expansion segments are highlighted with yellow. Those present in *S. cerevisiae* only are indicated by light blue arrows. rRNA domains are labeled with roman numerals.

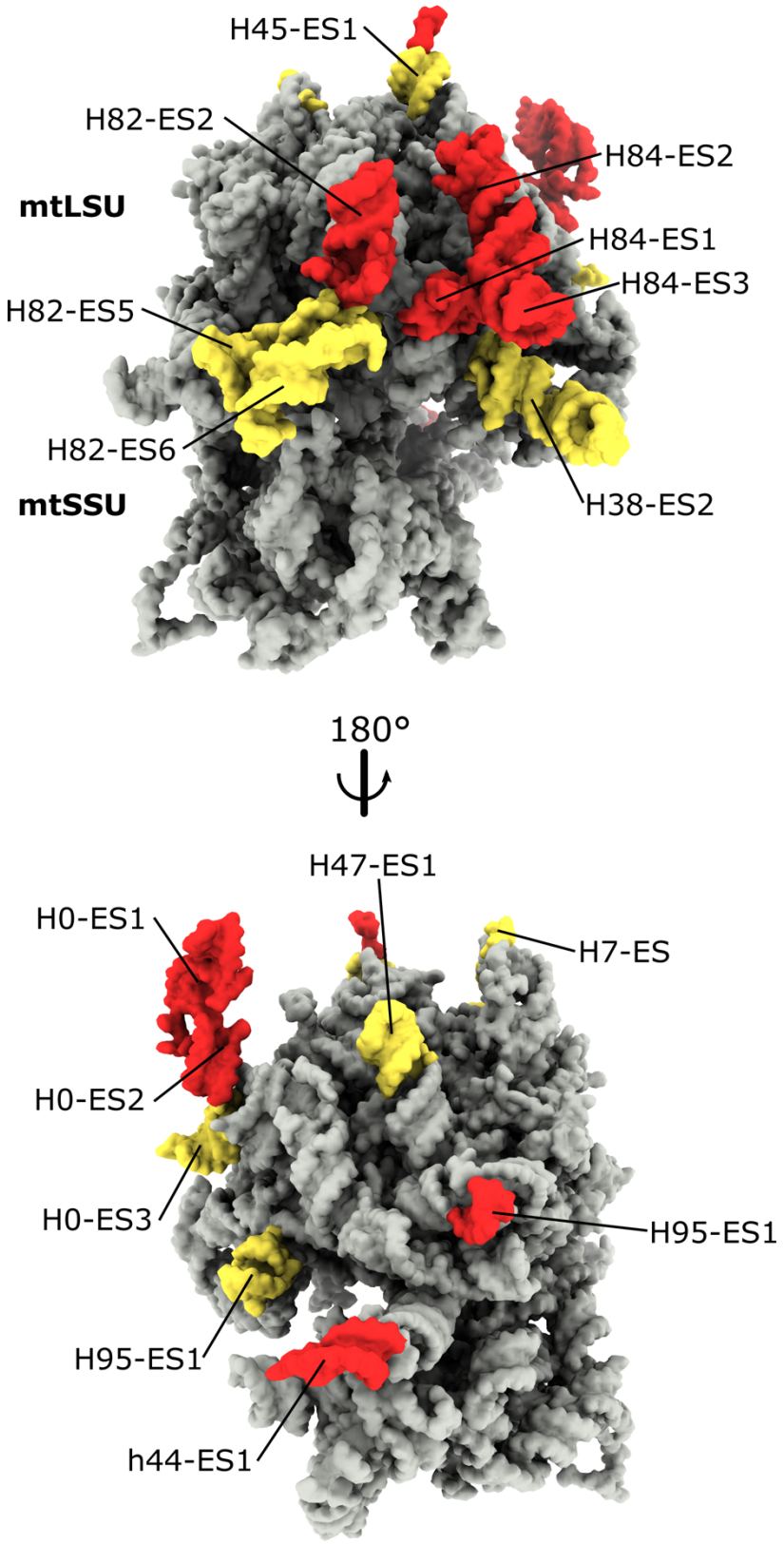


**Supplementary Figure 8. 3D view of the rRNA of mtLSU and mtSSU.** The conserved rRNA is in gray. ESs shared with *S. cerevisiae* are in red, and specific ESs in yellow.

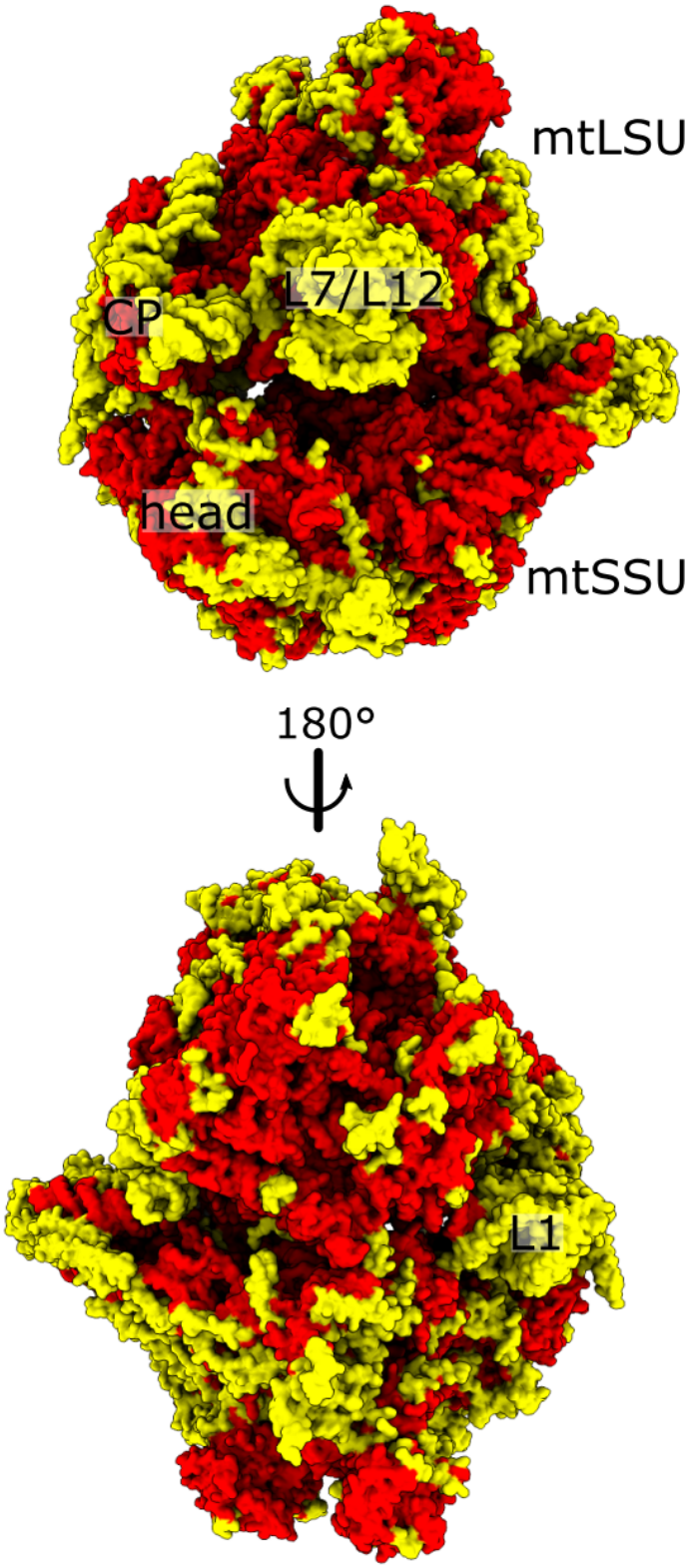


**Supplementary Figure 9. Improvements in the fungal mitoribosomal model.** The newly modeled and improved features in the current structure (yellow) compared with the previous model (red) of the *S. cerevisiae* mitoribosome (PDB ID: 5MRC).

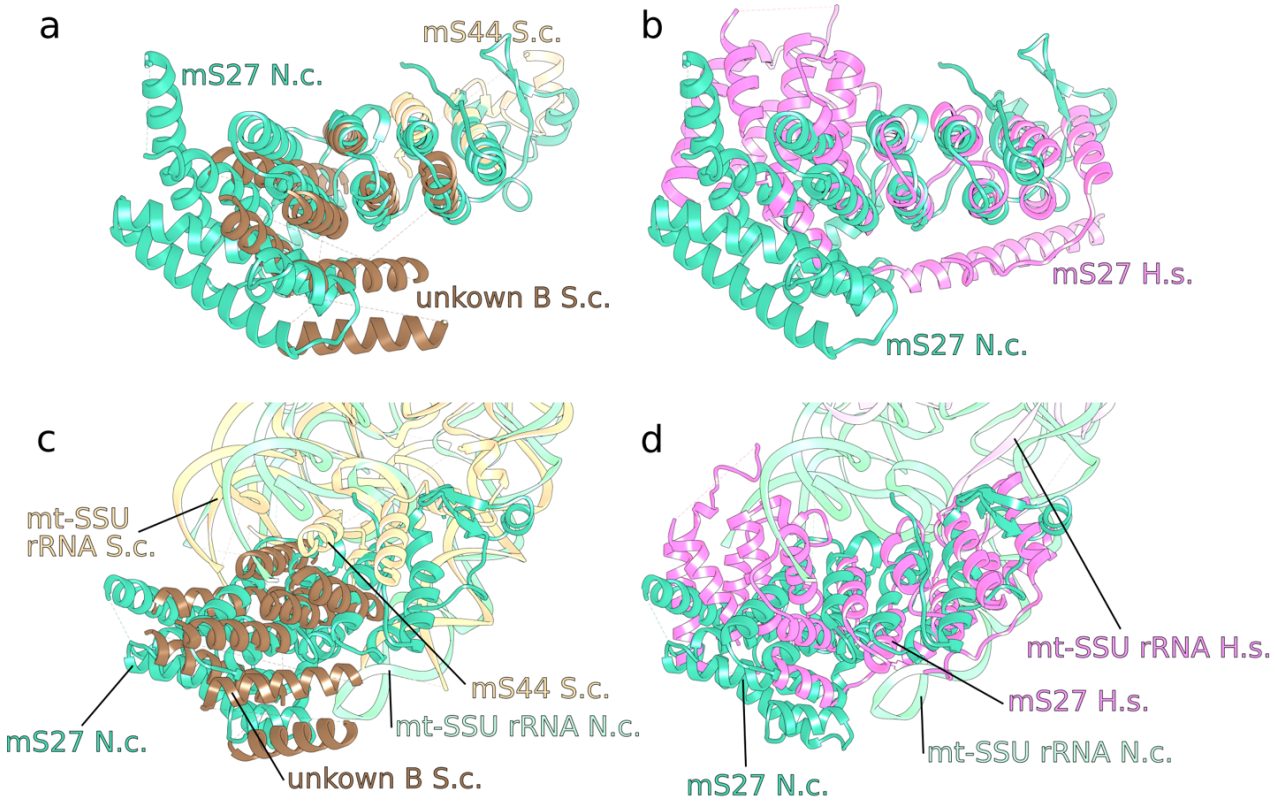


**Supplementary Figure 10. Superposition of mS27 orthologs. a,** *N. crassa* and *S. cerevisiae* mS27 is superimposed (previously assigned as mS44, 'unknown B'). **b,** *N. crassa* and *H. sapiens* mS27 is superimposed, showing similar fold. **c,** Superposition based on mtSSU rRNA suggests the same location form mS27 from *N. crassa* and *S. cerevisiae*. **d,** Superposition based on mtSSU rRNA suggests the same location form mS27 from *N. crassa* and *H. sapiens.*

a

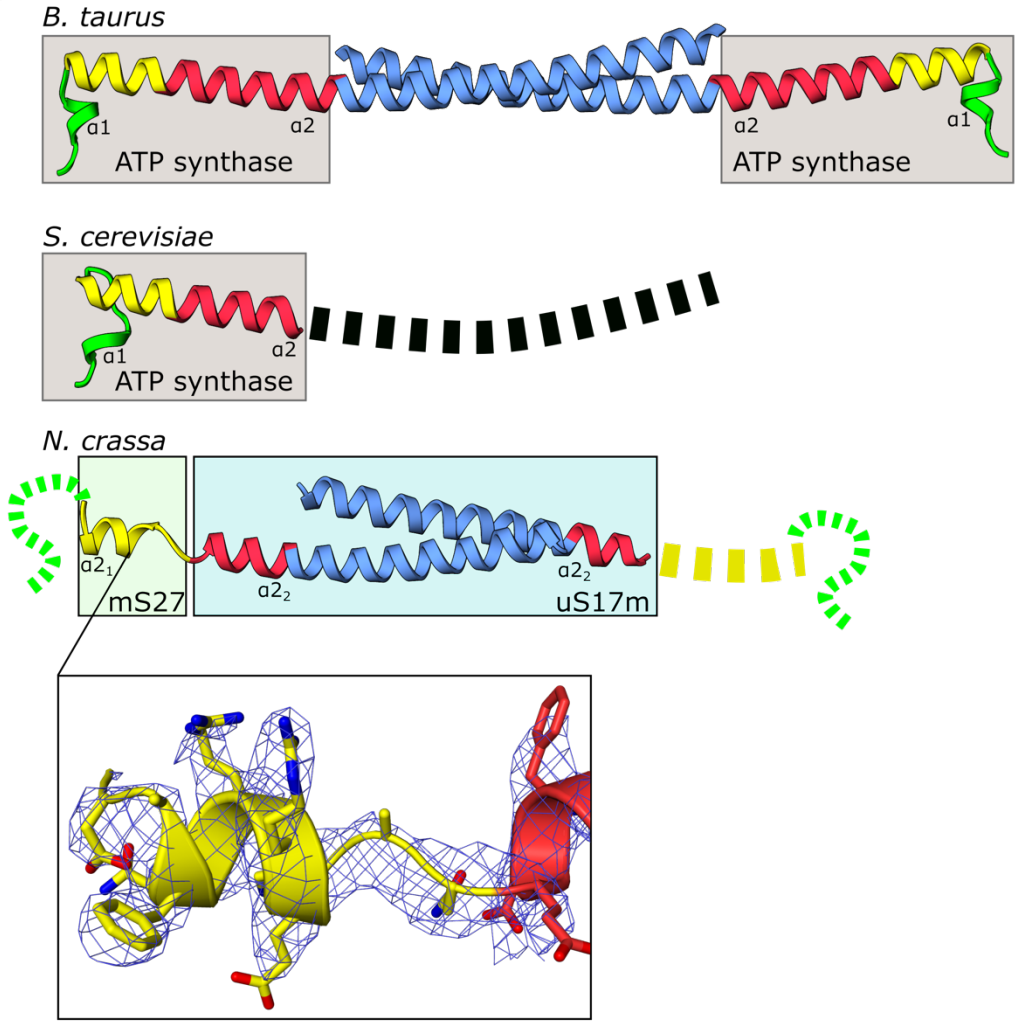
B. taurus
α1
α2
ATP synthase
α2
α1
ATP synthase
S. cerevisiae
α1
α2
ATP synthase
N. crassa
α2₁
mS27
α2₂
α2₂
uS17m

b

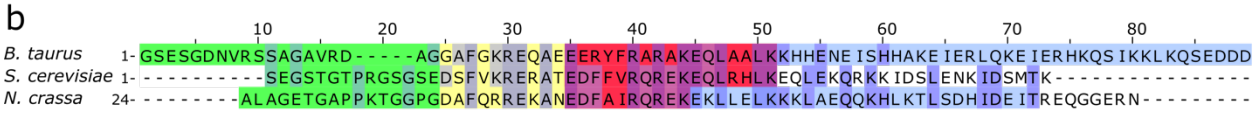
10 20 30 40 50 60 70 80
B. taurus 1- GSESGDNVRSSAGAVRD-----AGGAFGKREQAEEERYFRARAKEQLAALKKHHENEISHHAKEIERLQKEIERHKQSIKKLKQSEDDD
S. cerevisiae 1- ----------SEGSTGTPRGSGSEDSFVKRERATEDFFVRQREKEQLRHLKEQLEKQRKKIDSLENKIDSMTK----------
N. crassa 24- --------ALAGETGAPPKTGGPGDAFQRREKANEDFAIRQREKEKLLELKKKLAEQQKHLKTLSDHIDEITREQGGERN--------

c

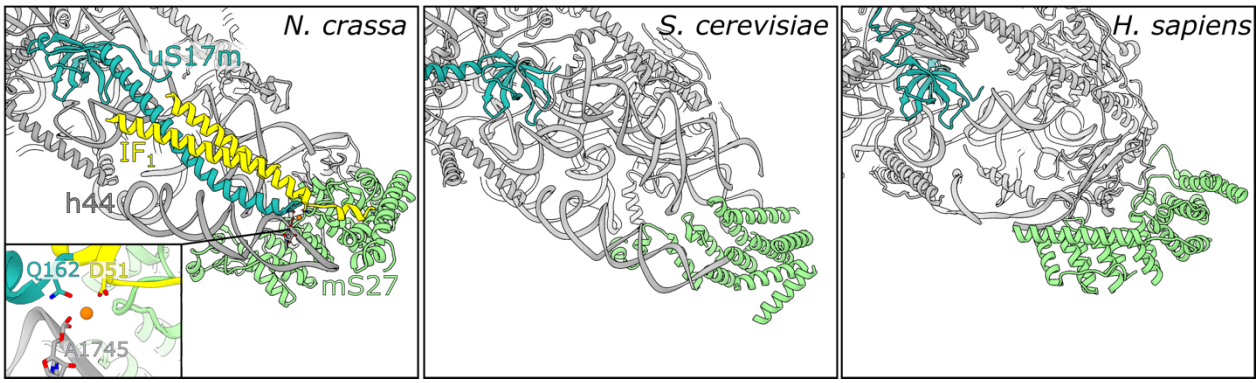
N. crassa
uS17m
IF₁
h44
Q162
D51
A1745
mS27
S. cerevisiae
H. sapiens

772

773

774 **Supplementary Figure 11. $IF_1$ topology, structure, binding and conservation. a**, $IF_1$ structure
775 is compared with those of *Bos taurus* (generated from PDB IDs: 1GMJ[17] and 4TFS[60]) and *S.*
776 *cerevisiae* (PDB ID: 3ZIA). Density map with model is shown to illustrate the quality of the data
777 in this region. The mitoribosome and $F_1$-ATPase binding parts are indicated with boxes. For *N.*
778 *crassa*, the disordered N-terminal region (residues 24-39), the short helix $\alpha2_1$ with a loop (residues
779 40-49), the longer helix $\alpha2_2$ outside the dimerization part (residues 50-58), and $\alpha2_2$ within the
780 dimerization part (residues 59-88) are colored as green, yellow, red, and blue, respectively.
781 Corresponding residues are colored accordingly in *B. taurus* and *S. cerevisiae*, where α1 is located
782 in the N-terminal region and $\alpha2_1$ and $\alpha2_2$ are a continuous helix α2. **b**, Structure-based sequence
783 alignment, colored as in **a**. The mitochondria targeting sequence is included in the residue
784 numbering for *N. crassa*. **c**, Structure of the $IF_1$-binding site of *N. crassa* mtSSU and the
785 corresponding regions from *S. cerevisiae* and *H. sapiens*. $IF_1$, uS17m, and mS27 are indicated. The
786 $IF_1$ homodimer forms a helical bundle with the specific C-terminal extension of uS17m. The Mg-
787 ion mediated bridge is shown in a zoom-in window.

788

789

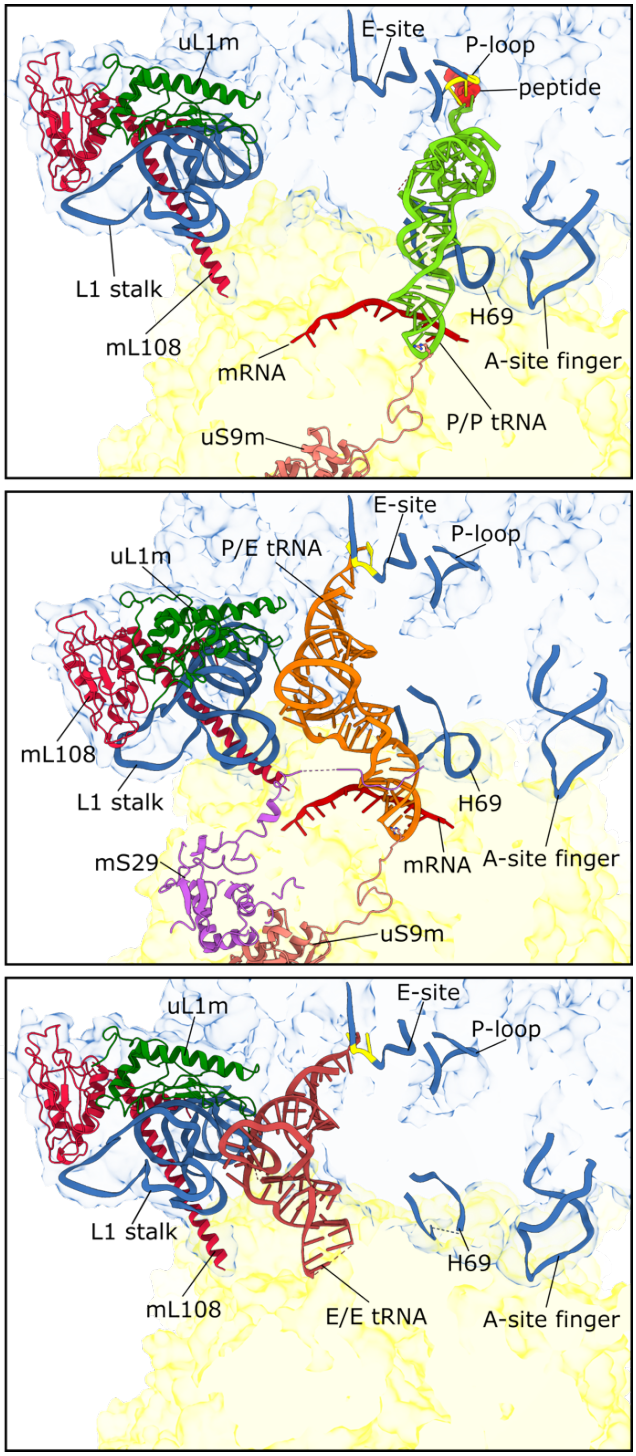


**Supplementary Figure 12. The L1-stalk and translocation of tRNA**. The three states are structurally aligned on mtLSU. Transparent surfaces of mtLSU and mtSSU are colored in blue and yellow respectively. Cartoon representations of important parts are shown and labeled. The P/P-tRNA state with the tRNA colored in green (top panel). The P/E-tRNA state with the tRNA colored in orange (middle panel). The E/E-tRNA state with the tRNA colored in red (bottom panel).

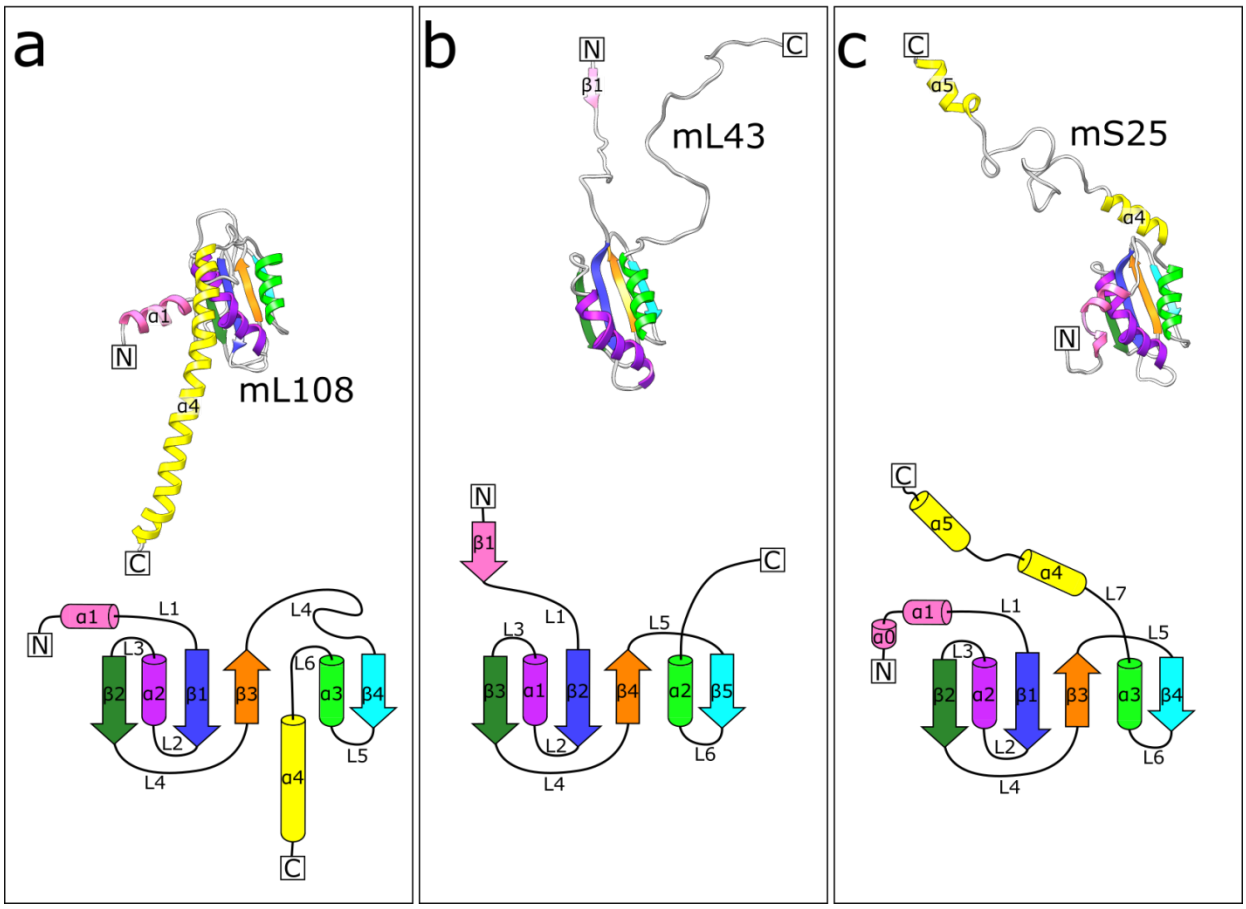


**Supplementary Figure 13. Topology of mL108, mL43, and mS25.** Three dimensional models and topology of the homologous proteins with secondary structure elements colored, featuring their structural similarity. **a,** mL108 of *N. crassa*. **b,** mL43 of *N. crassa* and **c,** mS25 of *Sus scrofa* (PDB ID: 5AJ4).

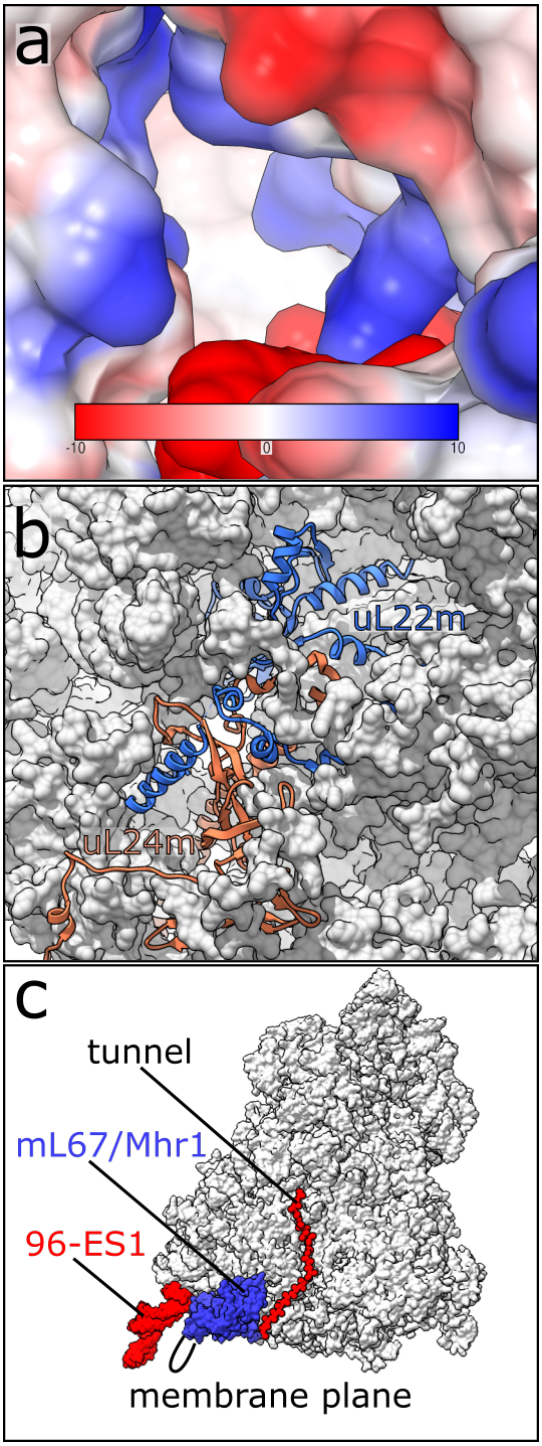


**Supplementary Figure 14. Analysis of potential exit sites of the poly peptide tunnel. a,** Surface representation colored by electrostatic Coulomb potential (kcal/mol*e) showing the view of the bacteria-like exit. The path is sterically restricted with positively charged protein environment. **b,** Surface representation of the *S. cerevisiae*-like exit. The path is sterically hindered by protein extensions of uL22m and uL24m, shown in cartoon. **c,** The polypeptide path in the *N. crassa* mitoribosome. The flexible elements 96-ES1 and mL67/Mhr1 extension around the exit are indicated.

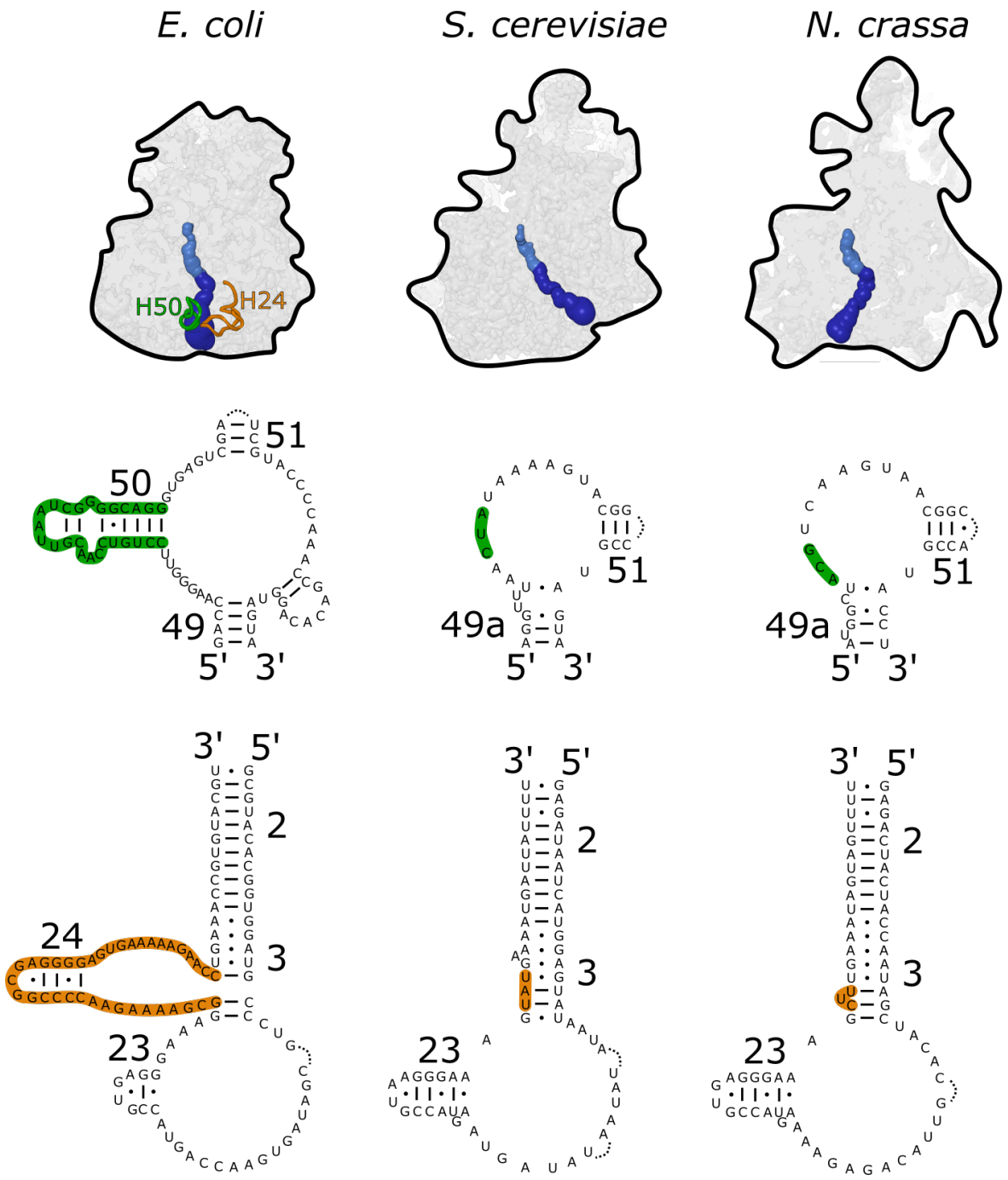


**Supplementary Figure 15. Comparison of the tunnel paths and the rRNA secondary structure elements involved in its formation.** The different tunnel paths are shown for the bacterial ribosome (*E. coli*) and the mitoribosomes from *S. cerevisiae* and *N. crassa*. The locations of the rRNA helices H24 (orange) and H50 (green) are indicated. The secondary structure diagram for H24 and H50 regions features their deletion from the sequence of the mitochondrial DNA in *S. cerevisiae* and *N. crassa.*

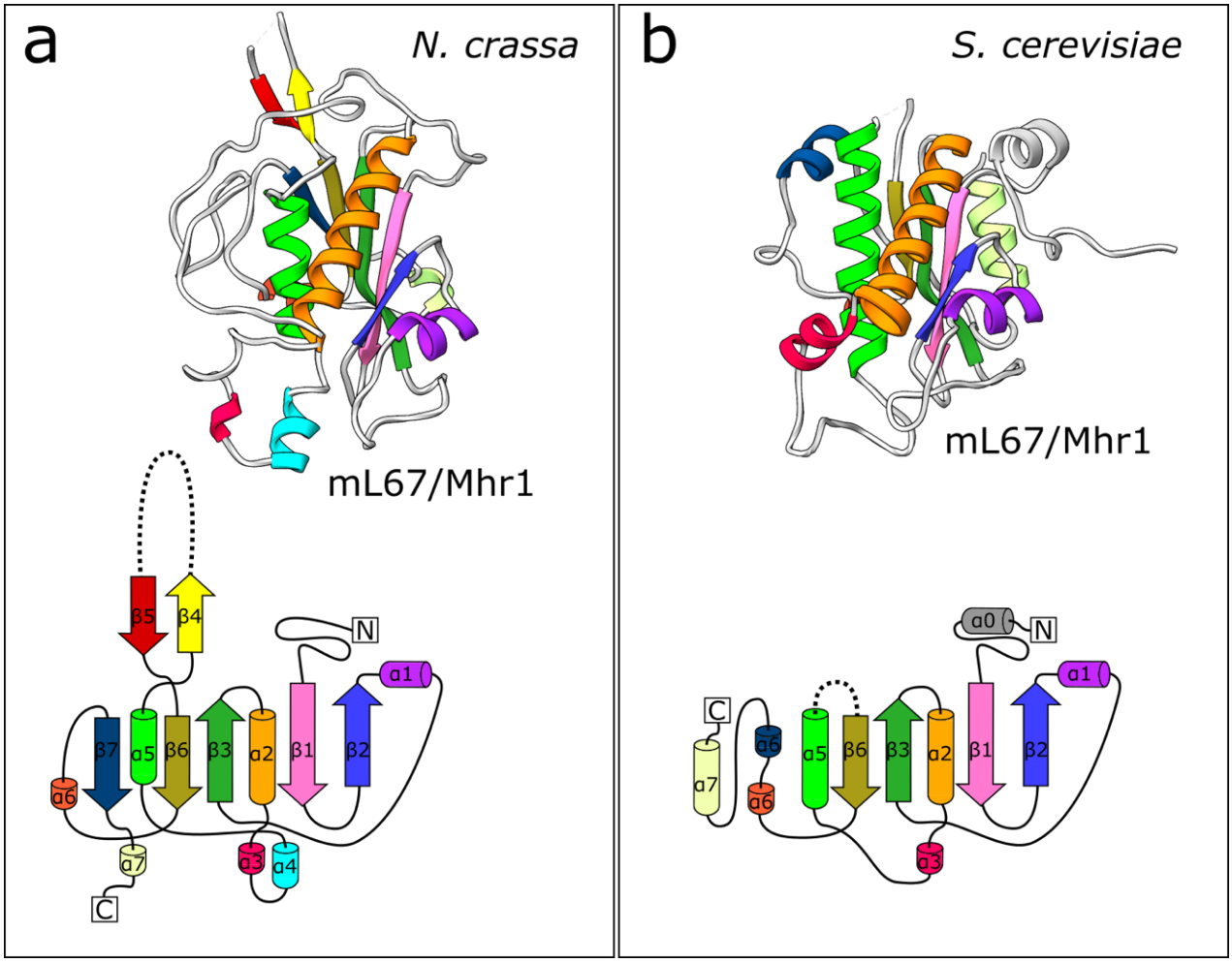


**Supplementary Figure 16. Structure and topology of mL67/Mhr1. a,** Three dimensional model and topology of *N. crassa* mL67/Mhr1 with secondary structure elements colored. The specific extension between β-strands 4 and 5 is indicated as dashed line. **b**, Three dimensional model and topology of *S. cerevisiae* mL67/Mhr1 following the same color scheme in panel a.

# Supplementary Tables

## Supplementary Table 1. Data and model statistics.

| **Data collection** | **mtLSU** | **mtSSU** | **Monosome with E-site tRNA** | **Monosome with P-site tRNA** | **Monosome with tRNA in P/E state** | **Late stage intermediate mtLSU (Atp25)** |
|---|---|---|---|---|---|---|
| Microscope | Titan Krios | Titan Krios | Titan Krios | Titan Krios | Titan Krios | Titan Krios |
| Detector | K2 Summit | K2 Summit | K2 Summit | K2 Summit | K2 Summit | K2 Summit |
| Magnification | 130,000 | 130,000 | 130,000 | 130,000 | 130,000 | 130,000 |
| Voltage [kV] | 300 | 300 | 300 | 300 | 300 | 300 |
| Total electron dose [$e^{-}/Å^2$] | 35 | 35 | 35 | 35 | 35 | 35 |
| Defocus range [μm] | −0.8 to −3.0 | −0.8 to −3.0 | −0.8 to −3.0 | −0.8 to −3.0 | −0.8 to −3.0 | −0.8 to −3.0 |
| Pixel size [Å] | 1.06 | 1.06 | 1.06 | 1.06 | 1.06 | 1.06 |
| Final particles | 131,806 | 131,806 | 23,802 | 24,611 | 37,908 | 24,142 |
| Resolution [Å] (overall/ LSU core / LSU CP / LSU L10 region / LSU L1 stalk / SSU head / SSU body / SSU tail) | 2.74/2.70/ 2.88/3.03/ 3.48/X/X/ X | 2.84/X/X/X/X/2.79/2.79 / 2.88 | 3.10/2.99/3.14/3.50/X/3.14/ 3.07/3.21 | 3.05/2.97/3.01/ 3.07/X/3.03/ 3.03/3.10 | 2.99/2.90/3.1 2/ 3.14/3.48/2.9 4/ 2.94/3.05 | 3.03/X/X/X/X/X/ X/X |
| Map-sharpening *B* factor [$Å^2$] (overall/ LSU core / LSU CP / LSU L10 region / LSU L1 stalk / SSU head / SSU body / SSU tail) | -50.7/- 48.3/- 69.6/- 74.4 /- 66.7/X/X/ X | -51.4/X/X/X/X/-48.3/- 56.5/-64.7 | -41.2/-33.6/ -60.9/-55.2/X/ - 50.4/-32.3/ -55.4 | -49.0/-36.8/ -46.0/-56.2/X/ -50.1/- 50.1/ -57.0 | -45.8/-46.1/ -55.9/-55.9/ -66.7/-41.1/ - 45.8/-61.0 | - 40.3/X/X/X/X/X/ X/X |
| **Model composition** | | | | | | |
| Total atoms (non-hydrogen/ hydrogen) | 223,408/9 7,527 | 167,560/76,668 | 390,797/173,689 | 392419/174345 | 394,205/175, 280 | 207,611/91,129 |
| Chains (RNA/ protein) | 1/44 | 1/37 | 3/78 | 4//79 | 4/80 | 1/42 |
| RNA residues | 2820 | 1435 | 4334 | 4362 | 4357 | 2529 |
| Protein residues | 8200 | 7528 | 15553 | 15604 | 15727 | 7802 |
| Metal ions ($Mg^{2+}$/ $K^{+}$/ $Zn^{2+}$) | 163/12/2 | 97/22/0 | 249/50/2 | 250/49/2 | 242/55/2 | 144/23/2 |

| | | | | | | |
|---|---|---|---|---|---|---|
| Ligands (ATP/ NAD/ spermine) | 0/1/1 | 1/0/0 | 1/1//1 | 1/1/1 | 1/1/1 | 0/1/1 |
| **Refinement** | | | | | | |
| Model to map CC ($CC_{mask}$/ $CC_{box}$/ $CC_{peaks}$/ $CC_{volume}$) | 0.84/0.74/0.71/0.82 | 0.86/0.72/0.66/0.84 | 0.81/0.77/0.75/0.80 | 0.83/0.78/0.77/0.82 | 0.84/0.79/0.78/0.83 | 0.81/0.76/0.74/0.79 |
| Average *B* factor [$Å^2$] ( protein/RNA/ metal ion and ligand/) | 172.29/170.34/75.62 | 95.19/121.44/36.55 | 117.81/173.91/83.19 | 56.92/82.51/38.83 | 69.33/102.72/29.15 | 68.65/131.13/25.77 |
| RMSD bond lengths [Å] | 0.002 | 0.002 | 0.002 | 0.002 | 0.002 | 0.002 |
| RMSD bond angles [°] | 0.382 | 0.357 | 0.373 | 0.354 | 0.362 | 0.402 |
| **Validation by MolProbity** | | | | | | |
| Clash score | 1.57 | 2.48 | 1.86 | 1.75 | 1.69 | 1.61 |
| Rotamer outliers [%] | 0.23 | 0.14 | 0.69 | 0.41 | 0.71 | 0.74 |
| Ramachandran plot [%] (Favored/ allowed/ disallowed) | 98.31/1.69/0.00 | 98.40/1.60/0.00 | 98.21/1.76/0.03 | 98.44/1.53/0.03 | 98.20/1.79/0.01 | 98.44/1.56/0.00 |
| **EMDB ID** (overall/ LSU core / LSU CP / LSU L10 region / LSU L1 stalk / SSU head / SSU body / SSU tail) | 10973/10974/ 10976/10975/X/X/X/X | 10958/X/X//X/X/ 10961/10962/ 10963 | 10978/10979/10981/ 10980/X/10982/ 10984/10983 | 10985/10986/10989/10988/X/10990/ 10991/10992 | 10965/10966/10968/ 10967/10971/10969/ 10970/10972 | 10977/X/X/X/X/X/X/X |
| **PDB ID** | 6YWS | 6YW5 | 6YWX | 6YWY | 6YWE | 6YWV |

845 **Supplementary Table 2. List of RNA and proteins from mtLSU.**

| Name | Gene | Uniprot ID | Chain ID | Modeled | Size | Notes |
|---|---|---|---|---|---|---|
| 23S rRNA | – | – | A | 2820 | 3464 | Spermine bound next to A1271. |
| uL1m | MRPL1 | Q1K699 | e | 59–300 | 303 | Conserved in *S. cerevisiae* and human but disordered in their structures. |
| uL2m | RML2 | Q7SCX7 | B | 54–379 | 383 | Likewise its *S. cerevisiae* counterpart, NT extension locates at the subunits interface. |
| uL3m | MRPL9 | Q1K8T6 | C | 63–369 | 384 | A helix at CT extension is similar to the human uL3m. This extension does not exist in the *S. cerevisiae* counterpart. |
| uL4m | YML6 | V5IMN1 | D | 62–302, 312–324 | 325 | |
| uL5m | MRPL7 | Q1K6P0 | E | 44–352 | 352 | |
| uL6m | MRPL6 | Q7RZF0 | F | 52–252 | 255 | |
| bL9m | MRPL50 | Q7S054 | G | 52–125 | 300 | |
| uL10m | MRPL11 | Q7RZ62 | f | 54–298 | 347 | Conserved in *S. cerevisiae* and human. It is not modeled in the *S. cerevisiae* structures. |
| uL11m | MRPL19 | Q7RX40 | g | 12–158 | 158 | Conserved in *S. cerevisiae* and human. It is not modeled in the *S. cerevisiae* structures. |
| uL13m | MRPL23 | Q7SBV6 | H | 1–183 | 183 | |
| uL14m | MRPL38 | Q7SBJ8 | I | 1–46, 59–131 | 131 | |
| uL15m | MRPL10 | Q7SB98 | J | 47–289 | 312 | |
| uL16m | MRPL16 | F5HIJ5 | K | 61–228 | 249 | |
| uL17m | MRPL8 | Q1K8C8 | L | 2–193 | 193 | CT extension unlike its *S. cerevisiae* counterpart lacking a helix. |
| bL19m | IMG1 | Q7RYW8 | M | 41–234 | 258 | |
| bL21m | MRPL49 | Q7SGE5 | N | 85–217 | 217 | |
| uL22m | MRPL22 | Q7S5N0 | O | 43–71, 122–364 | 364 | NT extension extensively remodeled with respect to its *S. cerevisiae* counterpart, whereas CT extension is quite similar. NT partially occupies the position of the absent bacterial rRNA helix 24. |
| uL23m | MRP20 | Q7SA60 | P | 13–192 | 228 | CT extension remodeled respective to its *S. cerevisiae* counterpart. |
| uL24m | MRPL40 | Q7RXU7 | Q | 1–353 | 396 | NT extension is a long helix that is not like its bacterial, *S. cerevisiae*, and human counterparts. CT extension is similar to that of the *S. cerevisiae*; it covers a long distance through the surface thereby connecting different parts of the large subunit. The CT extension compensates the absence of bacterial helices 15 and 16. |
| bL27m | MRP7 | Q1K730 | R | 67–196, 248–383 | 447 | NT extension is similar to bacterial, *S. cerevisiae* and human counterparts. CT extension extensively remodeled respective to *S. cerevisiae* bL27m, and partially interacts with rRNA helix 82. |
| bL28m | MRPL24 | Q7SC44 | S | 42–203, 209–225 | 274 | CT extension remodeled extensively respective to *S. cerevisiae* counterpart. |
| uL29m | MRPL4 | Q7S910 | T | 44–223 | 263 | |
| uL30m | MRPL33 | Q1K8Y7 | U | 2–102, 125–161 | 161 | |
| bL31m | MRPL36 | Q1K7L7 | V | 48–128, 189–207 | 219 | Bridging the mtLSU CP and the mtSSU head. |
| bL32m | MRPL32 | Q1K4P1 | W | 64–122 | 129 | Zn ion coordination. |
| bL33m | MRPL39 | V5IM60 | X | 7–54 | 59 | |
| bL34m | MRPL34 | Q96U95 | Y | 95–140 | 140 | |
| bL36m | RTC6 | Q7S4E7 | 0 | 79–124 | 124 | Zn binding |

| | | | | | | |
|---|---|---|---|---|---|---|
| mL38 | MRPL35 | Q7RXV8 | 1 | 83–449 | 449 | CT extension partially compensates the absence of bL35. Stabilizes helices 84-ES and 82-ES. |
| mL40 | MRPL28 | V5IQE0 | 2 | 248–370 | 370 | Stabilize helices 82-ES, 84-ES, 38-ES1. NAD is binding and interacting with mL40. |
| mL41 | MRPL27 | Q7S5W0 | 3 | 9–103 | 103 | |
| mL43 | MRPL51 | Q7S300 | 4 | 2–138 | 138 | |
| mL44 | MRPL3 | Q7SA88 | 5 | 55–237, 273–439 | 439 | NT extension slightly remodeled respective to *S. cerevisiae* mL44. CT extension interacts with helix 0-ES1. It forms heterodimer with mL57. |
| mL46 | MRPL17 | Q7S1Z3 | 6 | 82–245 253–303 311–368 | 368 | Interacts with helices 38-ES1 and 82-ES. |
| mL49 | IMG2 | Q7S518 | 7 | 82–165 | 165 | Most likely interacts with helix 28. |
| mL50 | MRPL13 | Q7S711 | 8 | 112–442 | 443 | Extensively remodeled. A 31 amino-acid long helix at the solvent-exposed surface of the protein. Interacting with helices 45 and 46. |
| mL53 | MRPL44 | Q7SGH0 | h | 1–98 | 98 | Conserved in *S. cerevisiae* and human. It is not modeled in the *S. cerevisiae* structures. |
| mL54 | MRPL37 | Q7SCZ3 | i | 77–118, 137–218 | 218 | Bridges L10/L11 area to CP. Conserved in *S. cerevisiae* and human. It is not modeled in the *S. cerevisiae* structures and only one helix is modeled in the human structures. |
| mL57 | MRPL15 | Q7S1R6 | 9 | 61–266 | 267 | Forms a heterodimer with mL44. Stabilizes helix 0-ES1. |
| mL58 | MRPL20 | Q1K6U7 | a | 41–103, 128–225 | 225 | Interacts with helix 0. |
| mL59 | MRPL25 | A0A0B0DMU6 | b | 2–162 | 162 | |
| mL60 | MRPL31 | U9W8F2 | c | 13–110 | 110 | |
| mL67 | MHR1 | Q7RYM5 | d | 33–218 243–291 | 292 | Similar to its *S. cerevisiae* counterpart with slight remodeling at NT and CT extensions. |
| mL108 | MRPL49 | Q7RWZ7 | j | 2-196 | 201 | Conserved but not modeled in *S. cerevisiae*. |
| Nascent polypeptide | – | – | cc | 7 | | |

846

847 **Supplementary Table 3. List of RNA and proteins from mtSSU.**

| MRP | Gene | Uniprot ID | Chain ID | Modeled | Size | Notes |
|---|---|---|---|---|---|---|
| 16S rRNA | – | – | aa | 1435 | 1864 | |
| bS1m | MRP51 | A7UWX2 | AA | 5–124, 132–213, 229–269, 288–337, 341–358, 368–430 | 470 | |
| uS2m | MRP4 | V5ILE0 | BB | 107–396 | 428 | |
| uS3m | VAR1 | P23351 | CC | 17–171, 193–369, 403–508 | 508 | |
| uS4m | NAM9 | Q7SA90 | DD | 1–215, 379–453 | 453 | |
| uS5m | MRPS5 | Q1K548 | EE | 56–180, 236–477 | 477 | Has a unique insertion to form a unique second beak. |
| bS6m | MRP17 | Q7SB95 | FF | 1–117 | 117 | |
| uS7m | RSM7 | Q7S6M9 | GG | 87–309 | 309 | |
| uS8m | MRPS8 | Q7SHF3 | HH | 2–161 | 161 | |
| uS9m | MRPS9 | Q7S7R6 | II | 69–315 | 315 | |
| uS10m | RSM10 | Q7RYL4 | JJ | 81–268 | 268 | |
| uS11m | MRPS18 | Q7SGU0 | KK | 253–376 | 376 | |
| uS12m | MRPS12 | Q7S9I4 | LL | 45–172 | 174 | |
| uS13m | SWS2 | Q7S2C2 | MM | 2–119 | 119 | |
| uS14m | MRP2 | Q7SF85 | NN | 2–113 | 113 | |
| uS15m | MRPS28 | Q1K5G1 | OO | 38–106, 114–320 | 320 | |
| bS16m | MRPS16 | P08580 | PP | 2–99 | 107 | |
| uS17m | MRPS17 | Q7S4E0 | QQ | 6–163 | 165 | A unique C–terminal helix, which binds the $IF_1$ dimer. |
| bS18m | RSM18 | Q1K8E0 | RR | 108–241 | 256 | |
| uS19m | RSM19 | Q1K8V2 | SS | 9–89 | 91 | |
| bS21m | MRP21 | Q7SAJ1 | TT | 149–236 | 236 | |
| mS23 | RSM25 | F8MRK5 | UU | 2–128, 142–238 | 240 | |
| mS26 | PET123 | Q7SHR9 | VV | 47–257, 262–287, 293–316 | 316 | |

| | | | | | | |
|---|---|---|---|---|---|---|
| mS27 | MRP13 | Q7RYW7 | WW | 40–270, 275–396 | 396 | Corresponds to mS27 in human. *S. cerevisiae* mS44 and the unknown B (PDB ID: 5MRC) are one connected protein, which corresponds to human and *N. crassa* mS27. |
| mS29 | RSM23 /DAP3 | Q7SD06 | XX | 57–66, 72–469 | 469 | DAP3 death associated protein 3. ATP and Mg ion are bound. |
| mS33 | RSM27 | Q1K5R0 | YY | 2–100 | 108 | |
| mS35 | RSM24 | Q1K5Z0 | ZZ | 42–353 | 382 | Has a unique N–terminal domain to form a unique beak. |
| mS37 | MRP10 | Q7S4Y4 | 11 | 2–89 | 90 | |
| mS38 | COX24 | Q7SHR6 | 22 | 312–344 | 344 | |
| mS41 | FYV4 | Q1K6Q3 | 33 | 43–235 | 236 | |
| mS42 | RSM27 /MRP1 | Q7S2H6 | 44, 55 | 43–302 | 310 | Homolog of Fe superoxide dismutase. Lost the catalytic Fe ion binding side. Two chains form a homodimer, in contrast to the mS42-mS43 heterodimer in *S. cerevisiae*. |
| mS45 | MRPS35 | Q7SHB2 | 66 | 66–348 | 348 | |
| mS46 | RSM28 | Q7SG49 | 77 | 223–401 | 414 | |
| mS47 | MRP5 /EHD3 | Q1K7A4 | 88 | 42–508 | 508 | 3-hydroxyisobutyryl-CoA hydrolase. Probably an active enzyme because its active site is conserved. |
| ATP–$IF_1$ | INH1 | V5IRA3 | 00, 99 | 39–86 | 95 | ATP synthase inhibitor 1. Forms a homodimer located in the mtSSU tail region. |
| tRNA | – | – | bb | 73 | | P, E or P/E tRNA state. The density is an average of different tRNA species. |
| mRNA | – | – | ee | 11 | | mRNA in the P and P/E state. The density is an average of different mRNAs. |

848

849 **Supplementary Table 4. Mass spectrometry analysis.** Purified mitoribosomes were analyzed,
850 and high-score non-mitoribosomal proteins are listed. Known translational proteins and the
851 components of the pyruvate dehydrogenase complex are excluded from the list for clarity. Newly
852 found components, mS27, mL108, $IF_1$, and Atp25, are highlighted in yellow.
853

| Uniprot code | Protein name | Score | #Peptide-to-spectrum matches | #Unique peptides | #Peptides | Coverage | Protein length (aa) |
|---|---|---|---|---|---|---|---|
| Q7RYW7 | mS27 | 886.51 | 245 | 18 | 18 | 51.77 | 396 |
| Q7RWZ7 | mL108 | 378.36 | 72 | 8 | 8 | 38.31 | 201 |
| Q7RVX2 | Hsp70 | 126.53 | 31 | 17 | 17 | 27.54 | 668 |
| P07038 | Plasma membrane ATPase | 114.18 | 30 | 13 | 13 | 19.46 | 920 |
| Q1K6B1 | T-box family protein | 105.90 | 29 | 11 | 11 | 14.00 | 1150 |
| Q7S5S5 | Stomatin family protein | 98.23 | 26 | 7 | 7 | 25.75 | 431 |
| V5IRA3 | $IF_1$ | 78.64 | 26 | 3 | 3 | 32.63 | 95 |
| Q872B4 | Pentatricopeptide repeat protein (uncharacterized) | 67.63 | 18 | 10 | 10 | 19.52 | 753 |
| Q7S8I8 | Uncharacterized protein | 61.27 | 16 | 10 | 10 | 16.48 | 1044 |
| P87224 | CoxI translation protein Cya5 | 59.58 | 16 | 13 | 13 | 16.55 | 1136 |
| A0A0B0E3A4 | Pentatricopeptide repeat protein (uncharacterized) | 59.57 | 14 | 11 | 11 | 20.24 | 830 |
| A0A0B0DXR5 | Band 7 like (uncharacterized) | 56.23 | 15 | 9 | 9 | 23.05 | 525 |
| Q7SER1 | 6-phosphogluconate dehydrogenase like (uncharactarized) | 48.25 | 12 | 6 | 6 | 18.73 | 550 |
| Q9HDH1 | AAA protease IAP-1 | 47.79 | 11 | 5 | 5 | 11.38 | 738 |
| A0A0B0DSS5 | Atp25 | 45.93 | 11 | 4 | 4 | 12.20 | 492 |

854